

Contents list available at CBIORE journal website

Remarkable Energy Development

Journal homepage: https://ijred.cbiore.id



Research Article

Optimization of the PVT performance with various orientations of jets and MFFNN-RSA prediction model for smart buildings

Ali Al-Otaibi^a, Ahmed Y. Hatata^{b,c}, Mansoor Alruqi^d, Aasem Alabdullatief, Mohamed A. Essa^{d,f*}

Abstract. The combined thermal and photovoltaic technology in PV/T systems is considered as a greatly promising technology for smart buildings. Thus, investigations for enhancing the PV/T performance are still proceeding. This research presents an investigation for novel configurations of cooling jets for the PVT system. The linear and circular distribution for the inlet jets considering regular and irregular positioning for all the jets as new cooling configurations are implemented. Moreover, the proposed geometrical configurations are optemized regarding the performance to identify the most suitable configuration that achieves the optimum efficiency and temperature. Furthermore, a novel hybrid ANN model is presented for predicting the performance of the PVT systems. This model combines the multi-feedforward neural network (MFFNN) with an optimization technique called reptile search algorithm (RSA). The proposed model can process the studied parameters to predict the PVT performance parameters (top surface temperature, temperature un-uniformity, outlet temperature, and efficiencies). The proposed MFFNN-RSA model minimized the mean square error to less than 0.4857·10⁻³. The maximum temperature decrease achieved by the presented configuration reached 60.62K compared to the uncooled case, while the minimum temperature un-uniformity reached 1K and 6K for 400 and 1000 W/m², respectively. The increase of the ambient temperature found to decrease the temperature un-uniformity in all the cases. The irregular jet with the linear distribution was found to achieve the optimum performance of the overall, thermal, and electrical efficiencies of 63.5%, 49.6%, and 14.25%, respectively. Furthermore, the electricity production cost was reduced by 11.6%, and the yearly CO₂ emissions were reduced by 215.3 kg/m² compared to the normal PV system. The proposed irregular-line distribution of the jets is found to be the best configuration regarding the temperature of the PV model and the overall efficiency considering the pumpi

Keywords: PVT; ANN; MFFNN; reptile search algorithm (RSA); co-generation; thermal efficiency; electrical efficiency.



@ The author(s). Published by CBIORE. This is an open access article under the CC BY-SA license (http://creativecommons.org/licenses/by-sa/4.0/).

Received: 18th February 2024; Revised: 6th April 2024; Accepted: 15th April 2024; Available online: 1st May 2024

1. Introduction

Photovoltaic systems are a compact and clean method for converting solar to electrical energy, as they account for 60% of renewable energy conversion in the world (Koohestani *et al.*, 2023). Using such systems participates in sustainability and reduces the carbon footprint created by traditional power generation systems. However, the increase in the PV temperatures negatively affects its efficiency. Different cooling techniques were proposed for enhancing the electrical efficiency (η_e) of the PV systems. Moreover, the harvested thermal energy from the cooling process could be counted as a by-product that increased the overall system efficiency (η_o) by up to 81% (Hasan *et al.*, 2018). With this high energy conversion efficiency, these systems can be considered as a compact and clean solution for hot water and electricity supply in smart cities. According to the cooling method, PV cooling methods are

classified into passive and active. Passive cooling considers fins and extending surfaces to enlarge the heat transfer, while active cooling applies forced convection. The active cooling type is usually more expensive than passive cooling as it needs pumping power. However, it achieves better performance than the passive cooling (Dwivedi et al., 2020) (Gharzi et al., 2020). The active cooling method applies many configurations to achieve forced convection. These configurations include serpentine, parallel flow channels, and impingement-jet flow. A cooling channel in which an inclined perforated plate is responsible for the flow distribution over the metal plate attached to the PV back was investigated numerically in (Zhang et al. 2022). For every 1×10⁻³ kg/s increase in the cooling mass flow rate (\dot{m}) , enhancements in the thermal efficiency (η_t) and η_e by 0.086% and 0.92%, respectively, were achieved. Furthermore, a forced airflow channel attached to the back side

^aDepartment of Civil Engineering, College of Engineering, Shaqra University, Dawadmi, 11911 Riyadh, Saudi Arabia.

^bDepartment of Electrical Engineering, College of Engineering, Shaqra University, Saudi Arabia.

^cElectrical Engineering Department, Engineering College, Mansoura University, Egypt

^dDepartment of Mechanical Engineering, College of Engineering, Shaqra University, Dawadmi, 11911 Riyadh, Saudi Arabia.

^eDepartment of Architecture and Building Science, College of Architecture and Planning, King Saud University, Riyadh 11421, Saudi Arabia.

^fDepartment of Mechanical Power Engineering, Faculty of Engineering, Zagazig University, 44519 Zagazig, Egypt.

of the PV-module was tested experimentally (Patil et al., 2023). Due to the forced convection air cooling, the PV average temperature (T_{av}) was reduced by 9°C, and η_e increased by 80% using \dot{m} of 0.08kg/s. Extra enhancement for the cooling process was tested using finned air flow channels (Özcan et al., 2021). Flat and curved fins with thicknesses of 1.5, 3, and 5 mm were investigated under an air velocity of 5 m/s. This could decrease the PV panel's temperature by 21°C with the flat fins. The curved fins caused higher pressure drops than the flat ones. The maximum electrical efficiency was found to reach 18.92%. Various baffle orientations in the air channel of a PVT system were tested numerically, as well, by (Song et al., 2023). The optimum orientation of the baffles achieved improvements in η_e and η_t by 4.3% and 12.9%, respectively. Aluminum fins were tested under different geometries as a heat sink for cooling the PV panel (Bayrak et al., 2019). Among the tested configurations of the fins, the optimum electrical efficiency achieved was 11.55%. A PVT system with underground pre-cooled air was investigated experimentally by (Elminshawy et al., 2019). The value of T_{av} was decreased by 13°C, and η_e was improved by 18.9%. A new idea for the PVT system was to partially cover a solar collector with a PV module (Kazemian et al., 2023). This achieved an improvement of 31.24% in the overall power output. Furthermore, it reduced the payback period of the system by 35.07% as per the PV system alone. Water spray was also applied to increase the relative humidity of air through a cooling channel attached to the PV Panel (Zhang et al. 2023). This achieved a reduction of approximately 17°C in T_{av}. An aircooled PVT system using a converging channel was tested experimentally and numerically (Baloch et al., 2015). Different convergence angles of the channel were tested in comparison with the uncooled PV case. A significant PV temperature reduction was noticed using the proposed converging channel. An improvement in η_e by 36.1% was achieved, and an economic study concluded that the cost was reduced 19.5% compared to the uncooled case.

A variety of systems use water as a cooling fluid (CF). This enhances the rate of heat transfer referring to the large specific heat of water and its various applications as hot water. A watercooled system with twisted tabs inside the riser tubes attached to the PV panel was tested experimentally (Kalateh et al., 2022). Both clockwise and counterclockwise twist directions were investigated. The use of the twisted taps in the riser tubes increased the energy efficiency by 28.4%. Water-propylene glycol as a CF was used in a cooling channel with small spaced dorsal-shaped transverse saliences through a numerical simulation by (Yildirim et al., 2022). The achieved η_e and η_t reached 17.79% and 76.13%, respectively. This test was conducted at the normal operating cell temperature (NOCT) conditions with a cooling fluid inlet temperature of 15°C and a flow rate of 0.014 kg/s. Although this study achieved very elevated η_t , it did not account for the pressure drop of the pumping power consumed.

As the flow direction affects the heat transfer process, the angle encountered between the temperature gradient and the velocity gradient is preferred to be smaller according to the field synergy theory (Shen *et al.*, 2021) (Li *et al.*, 2020) (Essa et al., 2023). One of the techniques that agrees with the synergy theory is the impingement-jet flow. An investigation was performed experimentally for the performance of the impingement jet nozzle cooling of the PV with different distributions, diameters, and nozzle to PV module spacing (Javidan & Moghadam, 2021). The nozzle-to-PV distance that achieved the best cooling for the PV was five times the nozzle diameter, which was the minimum value in this test parameter. This configuration decreased the

average PV temperature by around 30°C. The densest nozzle distribution achieved the best cooling effect for the PV. Moreover, with 0.014 kg/s of \dot{m} and a 4 mm nozzle-diameter, the jet cooling could achieve η_e and η_t of 10.2% and 82.3%, respectively (Khalaf et~al.,~2023). One of the normal flow solutions that presents a cheap manufacturing method is a perforated plate parallel to the PV in which the cooling stream passes through its holes normally on the PV module. An experimental indoor investigation was performed on the perforated plate to study its cooling effect for the PV module, using air as a CF (Ewe et~al.,~2022). The system achieved the optimum η_e and η_t of 10.36% and 57.3%, respectively.

Recently, machine learning (ML) methodologies, including artificial neural networks (ANNs), have proven their utility in modeling the performance of thermal and electrical systems like PV systems and heat exchangers. As a result, employing the ANN as a methodology for predicting the PVT systems' performance under various external and internal scenarios has been widely used recently. This includes; fluid \dot{m} , climate variations, and system design parameters that can be deemed appropriate (Gunasekar *et al.*, 2015) (Kalani *et al.*, 2017) (Ahmadi *et al.*, 2019).

The feed-forward neural networks (FFNNs) models were applied to estimate the PVT evaporator's performance in the heat pumps (Gunasekar et al., 2015). It used the relative humidity, wind speed, solar intensity, and air temperature, as inputs in the FFNN model. The model successfully predicted the PV cell temperature, efficiency, and evaporator heat gain. Different ANNs were used in (Kalani et al., 2017) for modeling the PVT with nanofluids as CF. The ANNs of the adaptive neuro-fuzzy inference system (ANFIS), Radial-basis function (RBFNN), and FFNN were applied to determine η_e of the PV, and the collector fluid outlet temperature. Also, the optimal structure of the networks was calculated by using the particle swarm optimization technique. Moreover, the genetic algorithm-back propagation (GA-BP) neural network model was employed to enhance the concentrated parabolic collector (CPC's) cavity absorber (Wei Wang Ming Li & Feng, 2017). Its objectives were to reduce the heat losses, enlarges the system's output energy and η_t . The results indicated that the GA-BP model accurately estimated the intricate nonlinear relation between the input/output parameters and surpassing the predective accuracy of other methods. Also, the Least Squares support vector machine (LS-SVM) and ANN were applied in the PVT systems' modelling and predict the thermal and electrical efficiencies (Ahmadi et al., 2019). The findings showed that the LS-SVM exhibited the most superior performance. Various PVT models were tested for the same conditions by using the FFNN (Al-Waeli et al., 2019). It tested the nanofluid/Phase change material (PCM), water-nanofluid PVT, water-based PVT, and conventional PV. The FFNN model proved that η_e and η_t were enhanced to 13.32% and 72%, respectively, by using nanofluid/nano-PCM. Also, it achieved mean square errors (MSEs) of 0.0282 and 0.0229 for the validating and training phases, respectively. Thermal and FFNN models were developed for performance prediction of various arrangements of the PVT connected with thermoelectric cooler (PVT-TEC) systems (Dimri et al., 2019). Three different configurations were studied: Aluminum/semitransparent-based PVT-TEC water collectors and opaque PVT-TEC collectors. The FFNN model was used to obtain the exergy efficiencies and the fluid temperature. Moreover, the FFNN was presented to model the nanofluid-based solar collector performance (Delfani et al., 2019). It used the reduced temperature difference, collector length, collector depth, nanofluid concentration, and flowrate to

predict the efficiency and thermal performance. Predicting both the Nusselt number and the collector's efficiency was obtained with a minimum mean absolute percentage error (MAPE) of 2.576% and 1.470%, respectively. The performance potential of various ANN models, such as LSTM, SOFM, SVM, SOVM, MLP, GFF, and RNN, was thoroughly reviewed and compared for data prediction in PVT collectors (Yousif et al., 2019). It was concluded that the transverse zone exposed to moderate/high irradiation, was deemed appropriate for the implementation of solar systems. The generated energy from the PVT based on nano-PCM, SiC-water, and nanofluid were enhanced in (Al-Waeli et al., 2020). The ambient temperature and solar irradiance were applied as inputs to the Self-organizing Feature Map and the MLP networks. According to the evaluation criteria, the models achieved an R2 value of 0.8742, an RMSE value of 0.149, an MSE value of 0.0223, and a trend accuracy of 59.7. A FFNN model was adopted to predict the PVT's efficiency in an air collector (Chaibi et al., 2021). The cell temperature and solar irradiance were used as inputs to the ANN model. Climatic samples of one year were used to train and validate the FFNN under various weather variables. The developed FFNN model showed MAPE of 0.0078% and 3.3607% in estimating η_e and η_t , respectively. Different ANN models were presented to optimize the efficiency of the nanocoolant PVT systems (Cao et al., 2022). Four ANNs, LS-SVM and ANFIS, were obtained by statistical and trial-and-error analyses. It used the irradiation intensity and the nanofluid flow rate as model inputs. The best prediction model was the ANFIS model for predicting η_e where it predicted 200 patterns for testing the model with MSE equal to 2.548, RMSE equal to 1.6, and R2 equal to 0.9534. Two distinct ANN models were presented for predicting the PVT performance parameters (outlet temperature, cell temperature, and exergy, thermal, and electrical efficiencies) (Büyükalaca et al., 2023). The models were specifically designed to utilize a cooling fluid of hexagonal BN/water nanofluid. In the first set of models, every model was created to forecast one specific performance parameter from the set of five. On the other hand, the second set of models employed an ANN model capable of predicting the five output parameters simultaneously. The FFNN-BP algorithm was consistently employed as a training algorithm across all models.

As can be deduced from the introduced literature, forced flow aligned normally with the PV interface achieves good cooling performance and elevated η_o of the system. The direction of the flow concerning the PV module plays an important role, and the normal flow of impingement jet flow cooling showed a good cooling effect in the thermal modules presented in the PVT systems. So, this paper studies the effect of varying the configuration of the jet flow considering different jet distributions, different distributions of the flow inlets and outlets in each jet distribution, and varying the flow and boundary test parameters. The paper presents the following contributions:

- Proposing a novel different configuration of jets on a cooling plate. This study presents both linear and circular distribution for the flow inlet jets over the cooling plate considering regular and irregular positioning for all the jets as new cooling configurations.
- The proposed distinct geometrical configurations are studied to identify the most suitable configuration that achieves the optimum efficiency and temperature.
- The different test parameters considered are mass flow rates, radiation intensities, wind speeds, and ambient temperatures.

- Building a numerical database using the optimum configuration considering wider ranges of the test parameters to be used as training material for the proposed ANN model.
- Proposing a novel MFFNN-RSA hybrid model to forecast the PVT system's performance as an application in smart cities.
- Using the proposed RSA to identify the most convenient parameters and architecture of the MFFNN model understudy.

2. Research Methodology

The research has a sequence of three different investigations. The first investigation performs a comparative study between four different jet flow configurations to identify the configuration with the optimum performance. The second investigation performs a study on the optimum configuration with wider test parameter ranges to constitute a numerical database for this configuration. In the third investigation, the proposed ANN model is trained and tested based on the created numerical database to make a predictive model for the best performance configuration.

2.1 The numerical model

The numerical model for the present study considered ANSYS Fluent and ANSYS ICEM software for solving the numerical model and building the mesh, respectively. The coupling of velocity and pressure is achieved through the utilization of the SIMPLE algorithm. The standard discretization is used for the pressure, while the first order is used for the turbulence and radiation model. Second-order upwind scheme is employed for the energy and momentum equations. The momentum, continuity, and turbulence equations employ a convergence criterion set at 1E-4, while the energy and radiation equations utilize a value of 1E-6. Finally, a steady-state solution is considered through all the numerical simulations.

2.1.1 Set of Equations

The set of equations discretized and solved in ANSYS Fluent software are the following equations (Ansys Inc, 2017):

Continuity equation:

$$\nabla \cdot (\rho \, \vec{V}) = 0 \tag{1}$$

where \vec{V} is the velocity vector in 3D space. Momentum equation:

$$\nabla \cdot (\rho \, \vec{V} \vec{V}) = -\nabla PP + \nabla \cdot (\bar{\tau}) + \rho \vec{g} \tag{2}$$

where PP is the pressure, and \vec{g} is the acceleration of gravity. \bar{t} is the stress tensor in the fluid domain.

The energy equation in the solid regions:

$$\nabla \cdot (\vec{V}\rho H) = \nabla \cdot (K_s \nabla T) \tag{3}$$

The Energy equation in the liquid regions:

$$\nabla \cdot \left(\vec{V}(\rho E + PP) \right) = \nabla \cdot \left(K_f \nabla T \right) \tag{4}$$

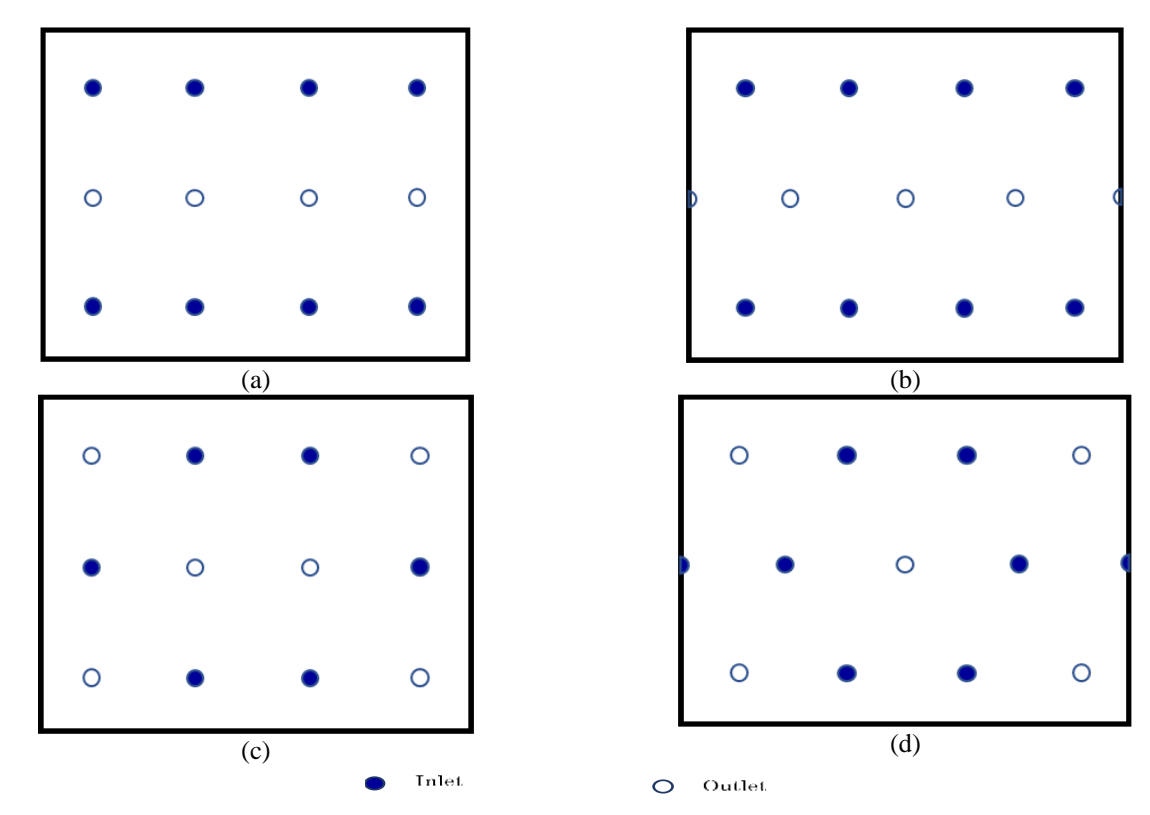


Fig 1. Jets distribution and inlets orientation for (a) Regular jets with linear inlets, (b) irregular jets with linear inlets, (c) Regular jets with circular inlets, and (d) irregular jets with circular inlets

where E includes the effect of the enthalpy (h), pressure energy, and kinetic energy in the flow. K_s and K_f represent the thermal conductivity for the solid and fluid regions, respectively. The model used for turbulence is the Renormalised group RNG k'- ϵ' model that as it is valid for high and low Reynolds number flows. k' is the kinetic energy of the turbulence, and ϵ' is the turbulence dissipation rate. The equations for both k' and ϵ' are expressed as follows:

$$\frac{\partial}{\partial x_i}(\rho k' V_i) = \frac{\partial}{\partial x_i} \left(\alpha_{k'} \mu_{eff} \frac{\partial k'}{\partial x_i} \right) + G_k - Y_{k'} \tag{5}$$

$$\frac{\partial}{\partial x_i}(\rho \varepsilon' V_i) = \frac{\partial}{\partial x_i} \left(\alpha_{\varepsilon'} \mu_{eff} \frac{\partial \varepsilon'}{\partial x_i} \right) + C_{1\varepsilon'} \frac{\varepsilon'}{K'} G_{k'} - C_{2\varepsilon'} \rho \frac{{\varepsilon'}^2}{K'}$$
 (6)

where $C_{1\varepsilon \prime}=1.42$, and $C_{2\varepsilon \prime}=1.68$. The values of $\alpha_{k\prime}$ and $\alpha_{\varepsilon\prime}$ are the inverse Prandtl numbers for k' and ε' , respectively.

The Discrete Ordinates (DO) radiation model was the radiation model implemented in the current study. The radiation equation is expressed as follows:

$$\frac{\mathrm{dIS}(\vec{\mathbf{r}},\vec{\mathbf{s}})}{\mathrm{ds}} + (a + \sigma_s)\mathrm{IS}(\vec{\mathbf{r}},\vec{\mathbf{s}}) = anr^2 \frac{\sigma T^4}{\pi} + \frac{\sigma_s}{4\pi} \int_0^{4\pi} \mathrm{IS}(\vec{\mathbf{r}},\vec{\mathbf{s}}) \Phi(\vec{\mathbf{s}}.\vec{\mathbf{s}}') d\Omega'$$
(7)

where IS(\vec{r} , \vec{s}) is the irradiance in position and direction vectors of \vec{r} and \vec{s} , respectively. a is the absorptivity, σ_s is the coefficient of scattering, nr is the index of refraction, and σ is the radiation constant of Stefan-Boltzmann, Ω' is the solid angle, and Φ is a phase function.

2.1.2 The Physical Domain

The PV module used in the present simulation is EGE-50P-36. On the backside of the module, a thermal module is installed with a thermal paste. The PVT model has dimensions of 520x680x23 mm. The properties and specifications of the materials used are described in Table 1 (Nahar *et al.*, 2017).

The jets distribution inside the thermal module considers regular and irregular orientations. Both configurations consider a horizontal and vertical spacing between the jets of 171.69 mm and 168.57 mm, respectively.

The diameter of the jet equals the spacing between the jet opening and the plate, which equals to 5mm. The selection of the inlet jets in these configurations considers linear and circular distributions. The difference between the four configurations is shown in Figure 1.

The boundary conditions of the model apply incident radiation on the top PV surface, with a combined convection/radiation heat loss. The backside of the thermal module and its sides are considered as adiabatic. The

Table 1Thermophysical properties of the PVT model understudy (Nahar et al., 2017).

Material	ρ , 33	K	Ср	Thickness
	[kg/m³]	[W/m. K]	[J/kg. k]	[mm]
Glass	2450	2	500	3.2
EVA	950	0.311	2090	8.0
PV Silicon	2329	148	700	0.5
Tedlar	1200	0.15	1250	0.1
Thermal paste	2600	1.9	700	0.3
Aluminium	2700	237	903	1
CF (water)	998	0.68	4200	17

convection coefficient (h_{conv}) is calculated according to the following relation (Shahsavar & Arıcı, 2023) (Duffie & Beckman, 2013):

$$h_{conv} = 2.8 + 3V_{wind} \tag{8}$$

where V_{wind} is the external wind speed. The rate of heat loss by convection [W/m²] is calculated as follows:

$$q_{conv} = h_{conv} * (T_{av} - T_{abm}) \tag{9}$$

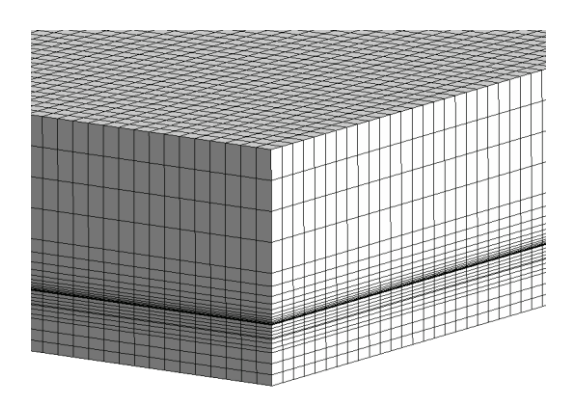
where T_{abm} is the ambient temperatures. The rate of heat loss by radiation [W/m²] is calculated as follows:

$$q_{rad} = e * \sigma (T_{av}^4 - T_{abm}^4) \tag{10}$$

Where e is the radiation emissivity.

2.1.3 Mesh generation and independence test.

The mesh was generated through Ansys ICEM software using a structured mesh of hexahedrons. A sample of the used mesh is shown in Figure 2. To ensure a mesh-independent solution, different meshes with different numbers of elements are used, and the top surface temperature is compared. This simulation is conducted for irradiance of 1200 W/m², 0.026 m/s fluid inlet velocity, an inlet fluid temperature of 293K, which is equivalent to ambient, and convection coefficient of 11.8 W/m²K. The variation of T_{av} with the different number of mesh elements is depicted in Figure 3. It is noticed that after 1.7 M elements, the value of the temperature is very near to that of the finest mesh at 3.3 M elements. So, in this paper, the mesh of 1.7 M is used for all the simulations.



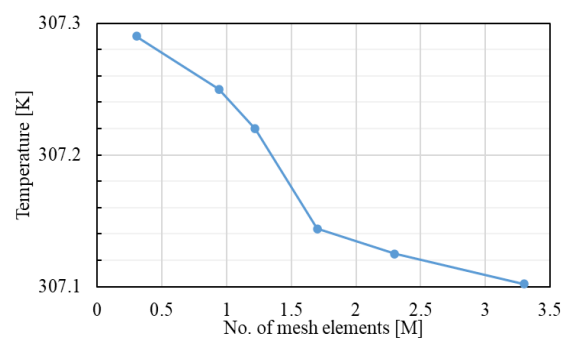


Fig 3. The PV temperature variation with the No. of elements in each mesh.

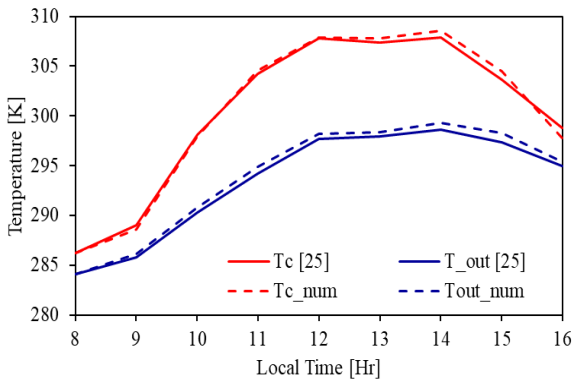


Fig 4. Comparison between experimental data from (Tiwari et al., 2006), and numerical simulation

2.1.4 Model Validation

The simulation model understudy is validated with experimental data for PV cooling with a back heat exchanger using air flow from (Tiwari *et al.* 2006). The comparison is conducted considering the outlet air temperature and T_{av} , as shown in Figure 4. It is observed that the results from the simulation highly agree with the experimental data with ARE of 4.12%.

2.1.5 Case setup

The setup for the boundary conditions on the different boundaries of the numerical model is illustrated on figure 5.

2.2 Performance Evaluation

The parameters used for judging the system's performance are η_e , η_{th} , and η_o . The electrical efficiency is evaluated according to T_{av} of the PV module (T_{av}) as follows:

$$\eta_e = \eta_{ref} \left(1 - \gamma \left(T_{av} - T_{ref} \right) \right) \tag{11}$$

where T_{ref} is the PV test temperature of 25°C, and η_{ref} is the PV module's temperature at this reference temperature, which equals to 0.14 for the used module. γ is the PV temperature decrease factor, which equals to 0.0041 /°C. According to the value of η_e , the electrical power (P_e) is calculated as follows:

$$P_e = \eta_e * IS * A \tag{12}$$

where IS is the incident irradiance, and A is the PV area.

The thermal efficiency, η_t , is the ratio between the harvested thermal energy and the input solar power. It is expressed as:

$$\eta_t = \frac{\dot{m} C_p (T_{ot} - T_i)}{\text{IS} * A}$$
 (13)

such that \dot{m} is the flow rate [kg/s], C_p is the specific heat of the CF, which is water in the present case, T_{ot} is the outlet temperature of the CF, and T_i are the inlet temperatures of the CF.

The overall efficiency is the ratio between all the produced electrical and thermal powers, considering the fluid pumping power loss ($\dot{Q}*\delta PP$), and the input solar power. This is expressed as follows:

$$\eta_o = \eta_e + \eta_t - \frac{\dot{Q} * \delta PP}{I * A} \tag{14}$$

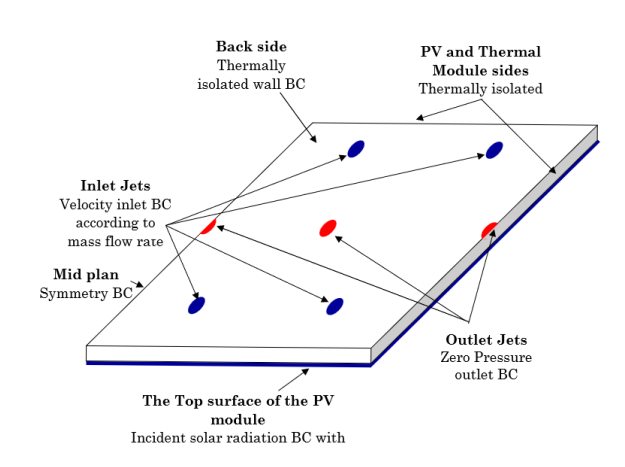


Fig 5. Boundary conditions on the Numerical model for the Irregular jets with linear inlets distribution case

One of the parameters used for judging the cooling efficiency and its homogeneity is the temperature non-uniformity (δT), which expresses the PV maximum and minimum temperatures expressed as follows:

$$\delta T = T_{max} - T_{min} \tag{15}$$

2.3 ANN model

The ANNs are widely recognized as a popular method in the field of artificial intelligence for modeling, predicting, and solving pattern classification problems. It typically contains three layers, which are output, input, and a layer of hidden sublayers. The appropriate number of these hidden sublayers is based on the degree of simplicity of the addressed problem. Neurons are the fundamental elements of the ANNs, that are like the neurons in the human brain. The neurons of the output and input layers rely on the number of the parameters in the outputs and inputs of the given problem, correspondingly. Each neuron in the ANN receives signals (inputs), perform a mathematical transformation to those signals, and produces an output signal (Talaat et al., 2020) (Abdel daiem et al., 2021) (Leema et al., 2016). Typically, the transformation within a neural network involves computing a weighted sum of the inputs, which is then followed by an activation function application. This activation function is responsible for presenting the non-linearity to the network. It determines the output of the neuron based on its inputs. During training, ANNs learn from labeled input-output pairs. The network adjusts its internal parameters, including the biases and weights linked to the neurons' connections, to reduce the error between the predicted and the desired outputs. This process is often achieved using optimization algorithms (Leema et al., 2016). Careful consideration is needed when determining who many neurons in the hidden layer, as it directly impacts the ANN performance.

2.3.1 Multi-layer feedforward neural network

In this paper, MFFNN is employed as the chosen ANN-based model. The network architecture consists of an input layer with four neurons (T_{amb} , I, \dot{m} , and h_{conv}) and an output layer with six neurons (T_{av} , δT , T_{ot} , η_e , η_t , and η_o). Optimizing the architecture of the MFFNN involves several considerations,

such as the appropriate activation functions, the number of hidden layers, the number of hidden neurons, and the hyperparameters (the learning rate, the batch size, and the optimization algorithms). Selecting the optimum architecture of the MFFNN will impact the capacity to learn the complex patterns, the training performance, and the network's ability to model the non-linear relationships (Talaat *et al.*, 2020). The first hidden layer output can be obtained by,

$$H_{i} = \frac{1}{[1 + \exp(-\sum_{j=1}^{m} (\omega_{ij} x_{j} - B_{i}))]} i = 1, 2, ..., N$$
 (16)

where x_j is the NN model input, and H_i is the output of the hidden neuron ith. m and N are the total neurons in the input and hidden layers, respectively. ω_{ik} and B_i are the weight factor and bias between jth input and ith hidden neurons, respectively. This equation will be repeated for the number of hidden sublayers in the proposed MFFNN model. The output layer outputs are calculated by,

$$O_k = \sum_{l=1}^{R} (\omega_{lk} H_l)$$
 k=1, 2, ...F (17)

where R and F are the total number of neurons in last hidden sublayer and the output layer, respectively. ω_{lk} is the weight factor between neuron l^{th} and neuron k^{th} in the hidden and output layer, respectively. O_k represents the output of k^{th} neuron in the output layer. The MSE function is used to evaluate the performance of the proposed MFFNN in this study (Abdel daiem *et al.*, 2021) (Leema *et al.*, 2016). The MSE is expressed as follows:

$$MSE = \frac{1}{M} \sum_{k=1}^{M} (O_k - A_k)^2$$
 (18)

where A_k is the actual output, and M represents the number of training patterns. The fitness function of training the proposed MFFNN model is determined by,

Fitness function = min (MSE) = Min.
$$\left[\frac{1}{M} \sum_{k=1}^{M} (O_k - A_k)^2 \right]$$
 (19)

The weights and biases of the proposed MFFNN are modified during the training by using the MSE function (Abdel daiem *et*

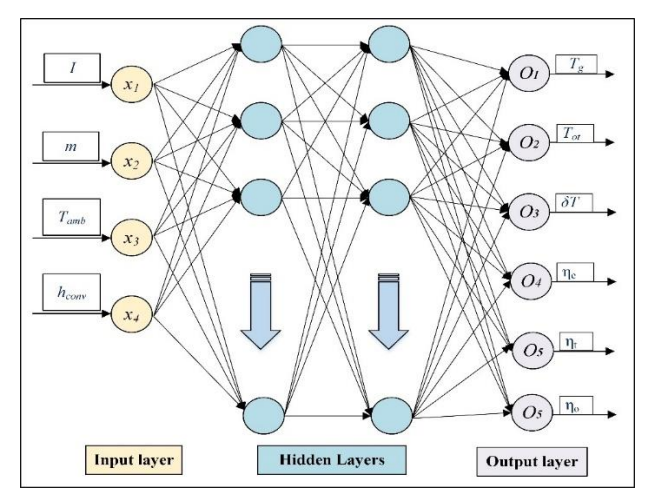


Fig 6. Proposed MFFNN structure

al., 2021). The optimization methods can be employed for training the MFFNN to find the optimum numbers of hidden layers, numbers of hidden neurons, activation functions, hyperparameters, and weights factors and biases. The reptile search algorithm (RSA) is used to attain the optimal architecture of the proposed MFFNN in the present study, Figure 6 illustrates the structure of the proposed MFFNN prediction model.

2.3.2 Reptile Search Algorithm

The RSA is an algorithm inspired naturally by metaheuristic algorithm that takes inspiration from the characteristics and behaviors of crocodiles. It relies on the hunting behavior, enveloping mechanism, and social dynamics observed in crocodiles. This swarm-based approach utilizes these principles to guide its search process (Abualigah *et al.*, 2022).

2.3.2.1 Generate initial solutions

The RSA initialization formula is used to generate the initial solution randomly within the solution domain. The solution domain represents the set of all possible solutions to the optimization problem (Abualigah *et al.*, 2022).

$$L_{ij} = LV + r.(UV - LV) \ j = 1, 2, ... n$$
 (20)

where L_{ij} is the value of the jth dimension of the ith crocodile. UV and LV upper and lower boundary values of the search domain, respectively. r is random number between 0 and 1, and n is the size of the populations.

2.3.2.2- Enveloping Mechanism

The RSA applies the concept of enveloping by exploring the search space in a way that focuses on promising regions while avoiding less favorable areas. This helps the algorithm efficiently navigate complex optimization landscapes. During the global search phase, crocodiles engage in elevated and sprawling walks. The search strategy can be calculated by iterations. The mathematical models of this mechanism can be modeled by (Abualigah *et al.*, 2022) (Khan *et al.*, 2023):

$$L_{ij}(t+1) = \begin{cases} L_{j,best}^{t} \cdot \left(-\vartheta_{ij}^{t} \times \beta \times R_{ij}^{t} \times r\right) & t \leq \frac{T_{m}}{4} \\ L_{j,best}^{t} \times L_{j,rand}^{t} \times ES^{t} \times r & \frac{T_{m}}{4} \leq t \leq \frac{2T_{m}}{4} \end{cases}$$
(21)

where t is the number of current iteration, T_m is the number of maximum iterations. $L^t_{j,best}$ is the optimum solution at t^{th} iteration and j^{th} location. ϑ^t_{ij} is the hunting operator value for i^{th} solution at j^{th} location. The hunting operator can be determined by:

$$\vartheta_{ij}^{t} = L_{j,best}^{t} \times \left(\sigma + \frac{L_{ij}^{t} - Avr(L_{ij}^{t})}{L_{i,best}^{t} \times (UV - LV) + \varepsilon}\right)$$
(22)

$$R_{ij}^{t} = \frac{L_{j,best}^{t} - L_{ij}^{t}}{L_{j,best}^{t} + \varepsilon}$$
(23)

$$ES^t = 2r_1 \left(\frac{T_m - 1}{T_m}\right) \tag{24}$$

where σ is a constant to control the accuracy of the exploration, r_1 is a random number from -1 to 1, ϵ is a minimum value to prevent the denominator from being zero, and Avr is the average value. ES is the evolutionary Sense.

2.3.2.3- Hunting Mechanism

The hunting mechanism is like an enveloping mechanism that has two phases: hunting cooperation and coordination. These phases are implemented to locate the best possible solution by exploring the search domain and assisting in capturing the prey. The two phases can be defined depending upon the iterations' number. Hunting coordination is applied for iterations from $t>0.5T_m$ to $t\le0.75T_m$. While the hunting cooperation is applied from $t>0.75T_m$ to $t\le T_m$. The following equations are used to represent the hunting mechanism (Abualigah et al., 2022) (Khan et al., 2023).

$$L_{ij}(t+1) = \begin{cases} L_{j,best}^{t} \times P_{ij} \times r & \frac{T_{m}}{2} < t \le \frac{3T_{m}}{4} \\ L_{j,best}^{t} - \vartheta_{ij}^{t} \times \varepsilon - R_{ij}^{t} \times r & \frac{3T_{m}}{4} < t \le T_{m} \end{cases}$$
(25)

2.3.2.4- Improved Reptile Search Algorithm

The RSA has some limitations, such as local minima trapping, high computational complexity, and slow convergence speed. Hence, in order to address these challenges, some modifications are presented for the original RSA. One adjustment involves integrating a sin operator into the high walking phase of the previous RSA algorithm. This modification is inspired from the sine cosine algorithm (Yuan *et al.*, 2022). The sin operator can avoid local minimum trapping and improve the capability of global exploration. The sin operator is inserted in (21) and modified as follows.

$$L_{ij}(t+1) = \begin{cases} L_{j,best}^{t} + \left(r_{2} \times \sin(r) \times \left| r_{3} \times L_{j,best}^{t} - L_{ij}^{t} \right| \right) & t \leq \frac{T_{m}}{3} \\ L_{j,best}^{t} \times L_{j,rand}^{t} \times ES^{t} \times r & \frac{T_{m}}{4} \leq t \leq \frac{2T_{m}}{4} \end{cases}$$
(26)

where r_2 and r_3 , are randomly selected numbers in range [0, 1]. The utilization of the chaotic inverse learning strategy by all individuals leads to higher computational costs and hindering algorithm convergence. To address this issue, this paper employs the linear decreasing population strategy. As the iteration progresses, the number of individuals utilizing the chaotic backward learning strategy gradually diminishes. The specific mathematical formula for implementing this strategy is outlined in (27).

$$P = r \times \left(\frac{(P_{min} - P_{max}) \times t}{T_m} + P_{max}\right)$$
 (27)

where P is the number of chaotic backward learning strategy populations. P_{min} and P_{max} are the minimum and maximum population numbers, respectively.

2.3.3 Proposed MFFNN-RSA hybrid model

The MFFNN proposed in this research undergoes training using the RSA technique, aiming to calculate the optimal architecture for various parameters, including the number of hidden sublayers, the number of hidden neurons, the biases and weights factors, and the activation functions. This optimized

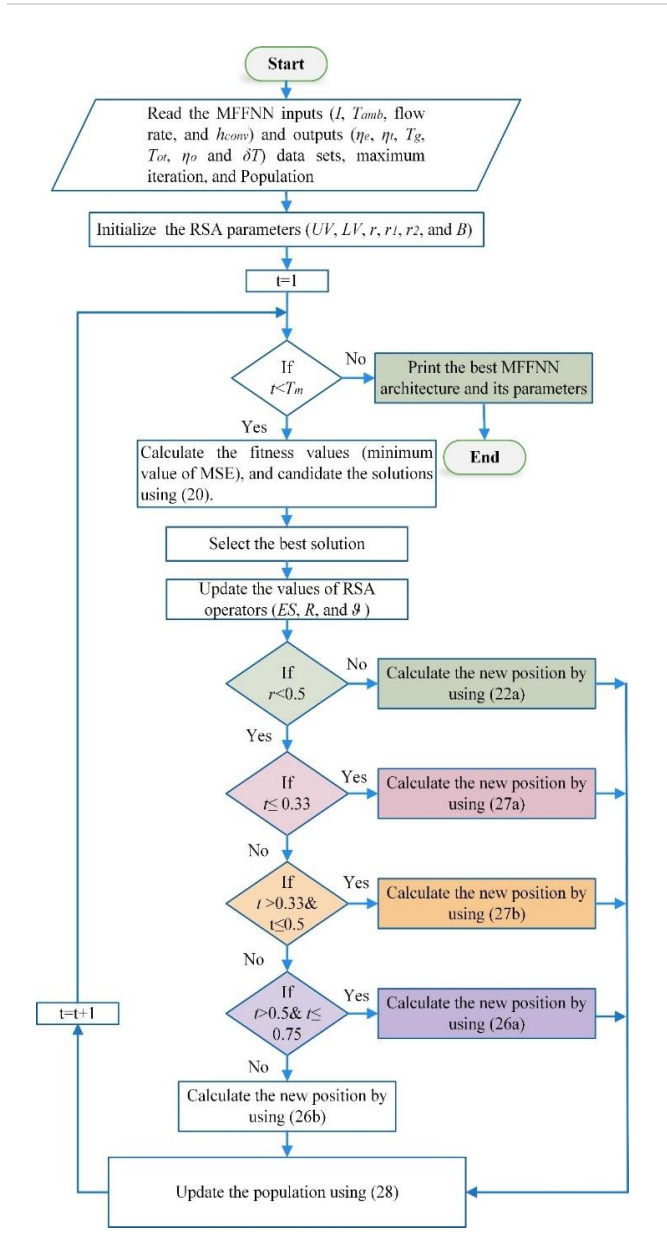


Fig 7. Flowchart of MFFNN-RSA model

MFFNN-RSA is subsequently employed to model and predict the PVT model's performance. The implementation of the proposed MFFNN-RSA layout is depicted in Figure 7 which can be outlined in the following steps:

- Firstly, the inputs of the proposed MFFNN are read, which
 consist of CF inlet temperature, mass flow rate, solar
 irradiance, and convection coefficient. The corresponding
 outputs to be predicted are the top surface temperature,
 temperature un-uniformity, outlet water temperature, and
 thermal, electrical, and overall efficiencies.
- Secondly, the parameters of the modified RSA are set. The modified RSA involves generating an initial population of locations randomly within specified upper and lower bounds. These locations are treated as potential solutions to the problem.
- Thirdly, the fitness function is then calculated for each location in the population using the MSE of the proposed MFFNN by using (20). The MSE serves as a measure of how well the MFFNN performs in predicting the desired outputs based on the given inputs.

- Fourthly, arrange the fitness values of all populations in ascending order, then evaluate the best locations of the crocodiles and update these locations using Equations (27 and 28). The improved positions of the crocodiles will serve as new solutions. If the constraints are achieved or the number of iterations reaches the maximum value, the crocodiles' locations will represent the optimal solution.
- Finally, the optimal results are displayed, including the number of hidden sublayers, the number of neurons within each hidden layer, the weights and biases factors, and the activation functions associated with the best crocodile locations. Figure 7 illustrates the flowchart of the proposed MFFNN-RSA hybrid model in detail.

The proposed MFFNN-RSA hybrid model is trained and tested using a group of 100 patterns. These patterns are collected and then fed into the model to obtain the optimal architecture of the MFFNN. The training process of the MFFNN-RSA hybrid model is implemented using a MATLAB program (version 2020). A specific m-file is created to handle the training process of the MFFNN, while the ANN toolbox is utilized to model the proposed MFFNN. By applying the proposed RSA technique, the MFFNN-RSA hybrid model can determine the most suitable architecture for achieving the desired outcome.

3. Results and discussion

This section explores the results and discussion of the three tests presented in this paper. This includes the comparison among the four proposed PVT models viewed in figure 1, the results of the performance for the optimum model among the four presented with more parameter ranges, and the third of the MFFNN-RSA hybrid model.

3.1 Modules Comparison results and discussion.

In this section, the temperature contours, temperature nonuniformity, and the performance indicators of the different efficiencies are presented. The parameters tested in this test are solar irradiance of 400 and 1200 W/m² and wind speed of 0 and 3 m/s, which are equivalent to convection coefficient of 2.8 and 11.8 W/m².K, respectively. And \dot{m} of 0.003135 and 0.028218 kg/s.

3.1.1 Temperature Contours and Flow Streamlines.

The temperature contours of T_{av} with test conditions of 1200 W/m² of irradiance, T_{amb}=T_i=293K, and convection coefficient of 2.8 W/m².K for **m** of 0.003135 kg/s and 0.028218 kg/s are shown in Figure 8. The maximum temperature of the regular and irregular line distribution reaches 315.7K and 314.5K, respectively at low cooling flow rates, as observed in the subfigures (a) and (b). at the high flow rates, the maximum temperature of the regular and irregular line distribution reaches 302.3K and 301.7K, respectively, as indicated in the subfigures (e) and (f). This temperature decrease is caused by increasing the convection due to the cooling flow rate. For the regular and irregular circle distribution, the maximum temperatures reach 320.1K and 319.8K, respectively for low flow rates, as indicated in the subfigures (c) and (d). for the higher flow rates, this maximum temperature reaches 305.9K and 305.8K for the regular and irregular circle distributions, respectively, as indicated in the subfigures (g) and (h).

It is observed that the line-distributed jets in the regular or irregular orientation achieve a lower maximum temperature

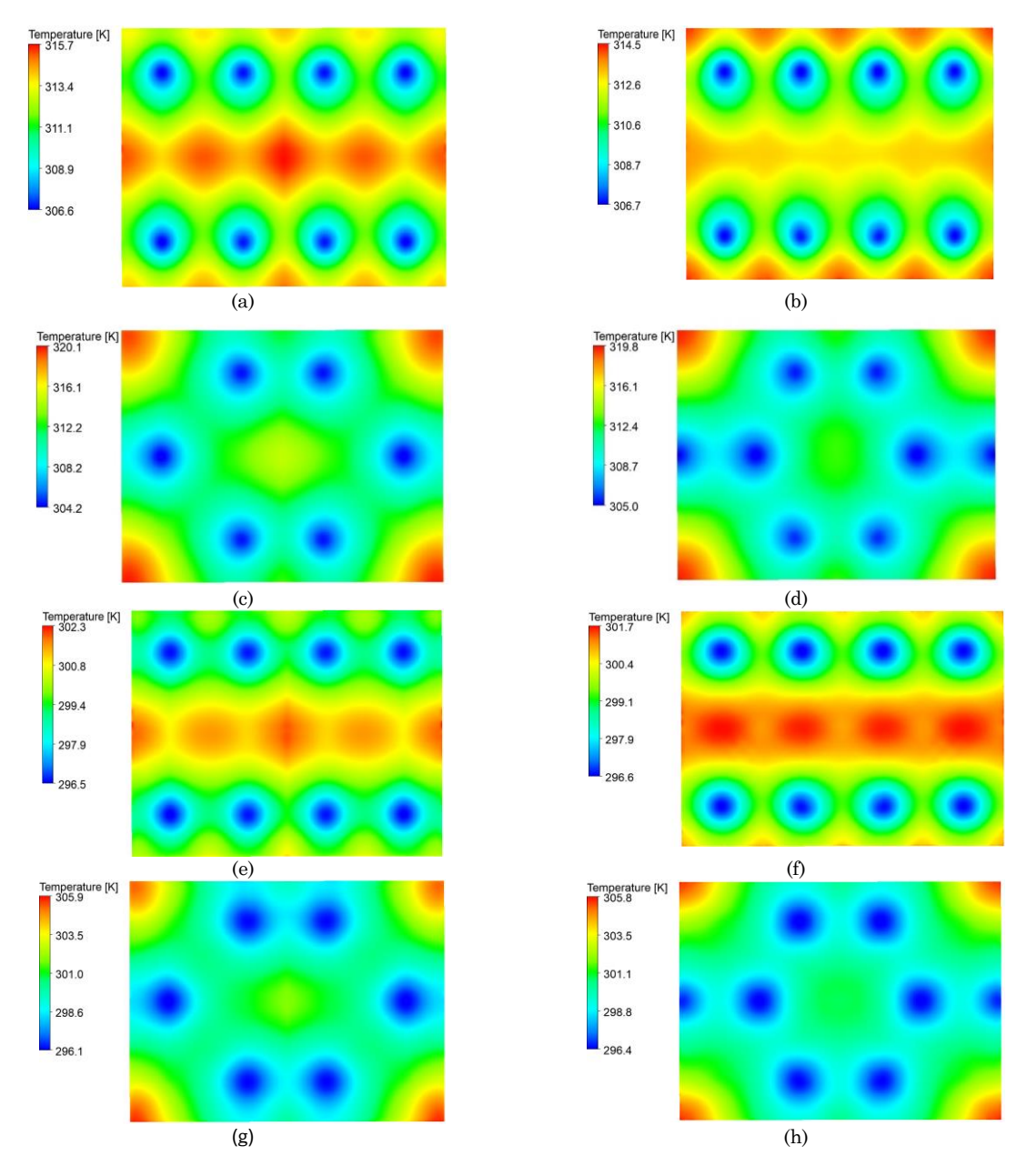


Fig 8. Temperature contours for the PV surface under \dot{m} of 0.003135 kg/s for (a) Regular- line jets distribution, (b) Irregular- line jets distribution, (c) Regular- circle jets distribution, and (d) Irregular- circle jets distribution. And under \dot{m} of 0.028218 kg/s for (e) Regular- line jets distribution, (f) Irregular- line jets distribution, (g) Regular- circle jets distribution, and (h) Irregular- circle jets distribution

than the circle distribution in both flow rates. This refers to the distribution of the inlet flow rate on eight jets in the case of the line distribution. However, the inlet jets are 6 and 7 only in distribution the regular and irregular circular distributions, respectively. This larger number of inlet jets permits a more effective distribution of cooling over the panel. It can be noticed that the irregular distribution of the jets achieves lower temperatures in the line distribution for the nature of the irregular distribution of the jets. At higher flow rates, as indicated in subfigures (e), (f), (g) and (h), the PV temperature decreases more than the low cooling flow rates due to the higher convection coefficient in the cooling channels.

Figure 9. shows the shape of the flow streamlines for the four flow configurations in the present test set. It can be observed that the line distribution of inlet jets represented by

Figure 9. (a) and (b), guarantees the distribution of the streamlines fairly over the whole area, with small regions clear from the streamlines. This reflects a good contact of the CF flows through these streamlines to the panel and that the cooling effects reach larger areas. This explains the lower temperatures achieved by this distribution. However, the circular distribution leaves larger areas with no streamlines, thereby indicating that these regions are not affected well by the cooling process.

3.1.2 Average temperature of the PV module

Figure 10 shows variation of T_{av} of the tested cases with an ambient temperature of 293K and 313K under different irradiance power, convection coefficient and \dot{m} . It can be observed that the case of irregular circle configuration of the jets

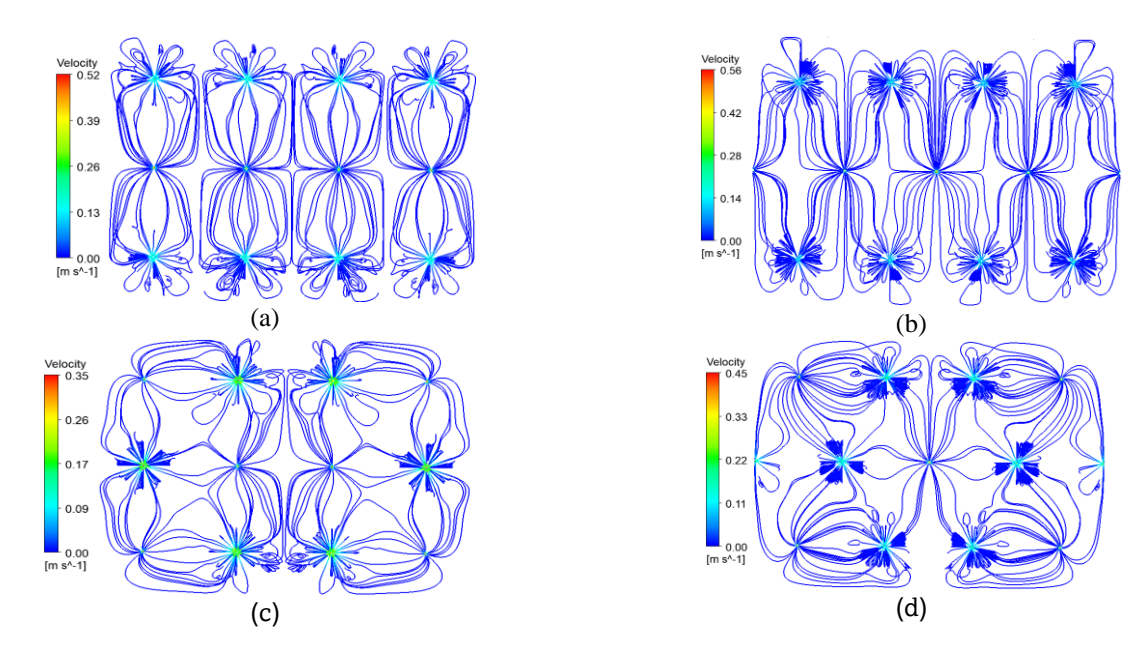
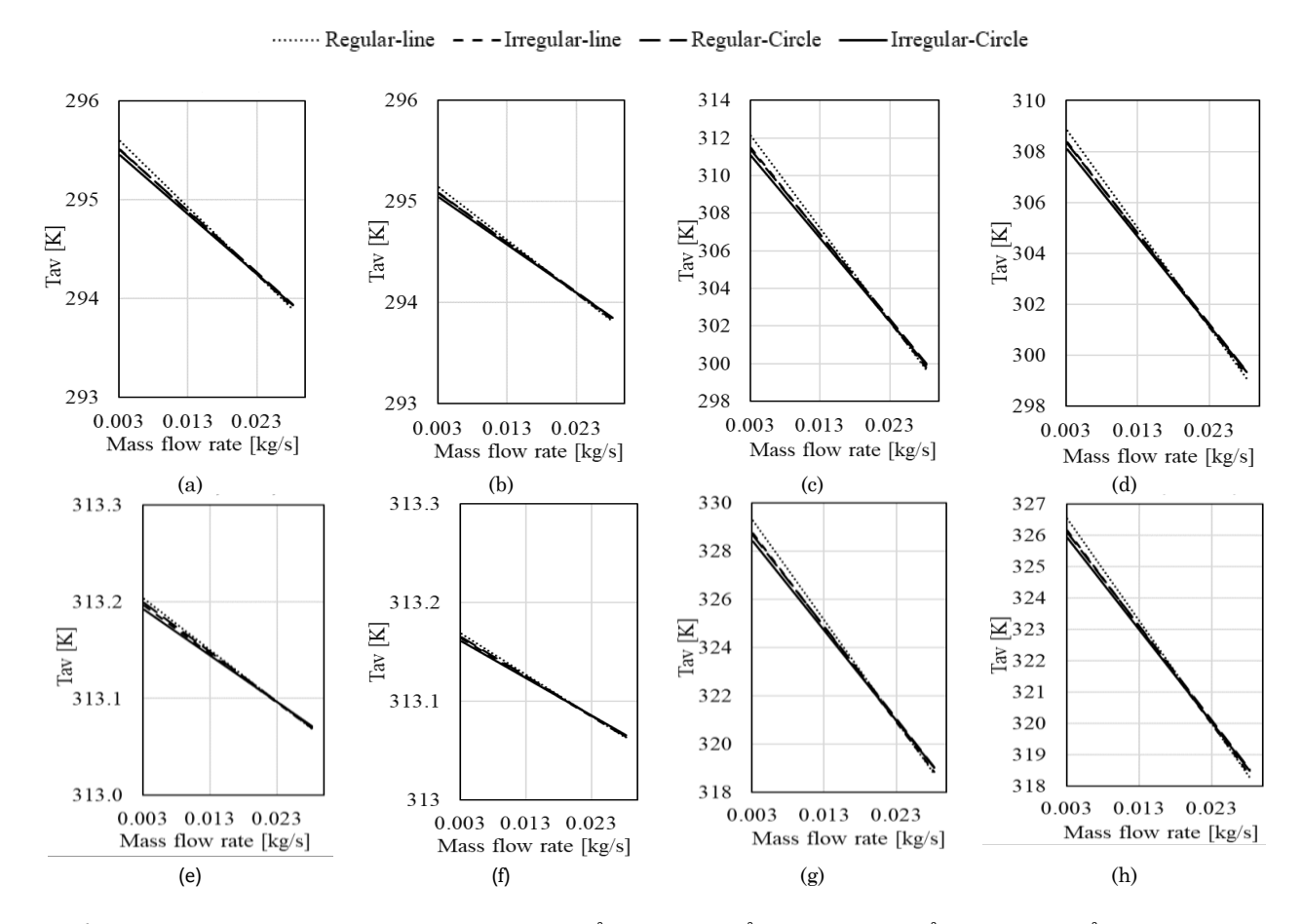


Fig 9. Streamlines under \dot{m} of 0.028218 kg/s for (a) Regular-line jets distribution, (b) Irregular-line jets distribution, (c) Regular-circle jets distribution, and (d) Irregular-circle jets distribution.

achieves the lowest average temperature at low flow rates, which reaches 295.45K. In comparison, the regular line configuration reaches the lowest average temperature of 293.89K at high flow rates as observed from the subfigure (a). It

is evident that by increasing \dot{m} , the temperature decreases in all cases. Moreover, the increase of the convection coefficient caused by the moving air around the panel helps decrease the average temperature, as observed in cases (b) and (d) compared



 $\begin{tabular}{l} \textbf{Fig 10}. T_{av} behaviour at T_{amb}=293K under (a) IS=400 W/m^2, h_{conv}=2.8 W/m^2.K, (b) IS=400 W/m^2, h_{conv}=11.8 W/m^2.K, (c) IS=1200 W/m^2, h_{conv}=2.8 W/m^2.K, and at T_{amb}=313K under (e) IS=400 W/m^2, h_{conv}=2.8 W/m^2.K, (f) IS=400 W/m^2, h_{conv}=11.8 W/m^2.K, (g) IS=1200 W/m^2, h_{conv}=2.8 W/m^2.K, and (h) IS=1200 W/m^2, h_{conv}=11.8 W/m^2.K.} \end{tabular}$

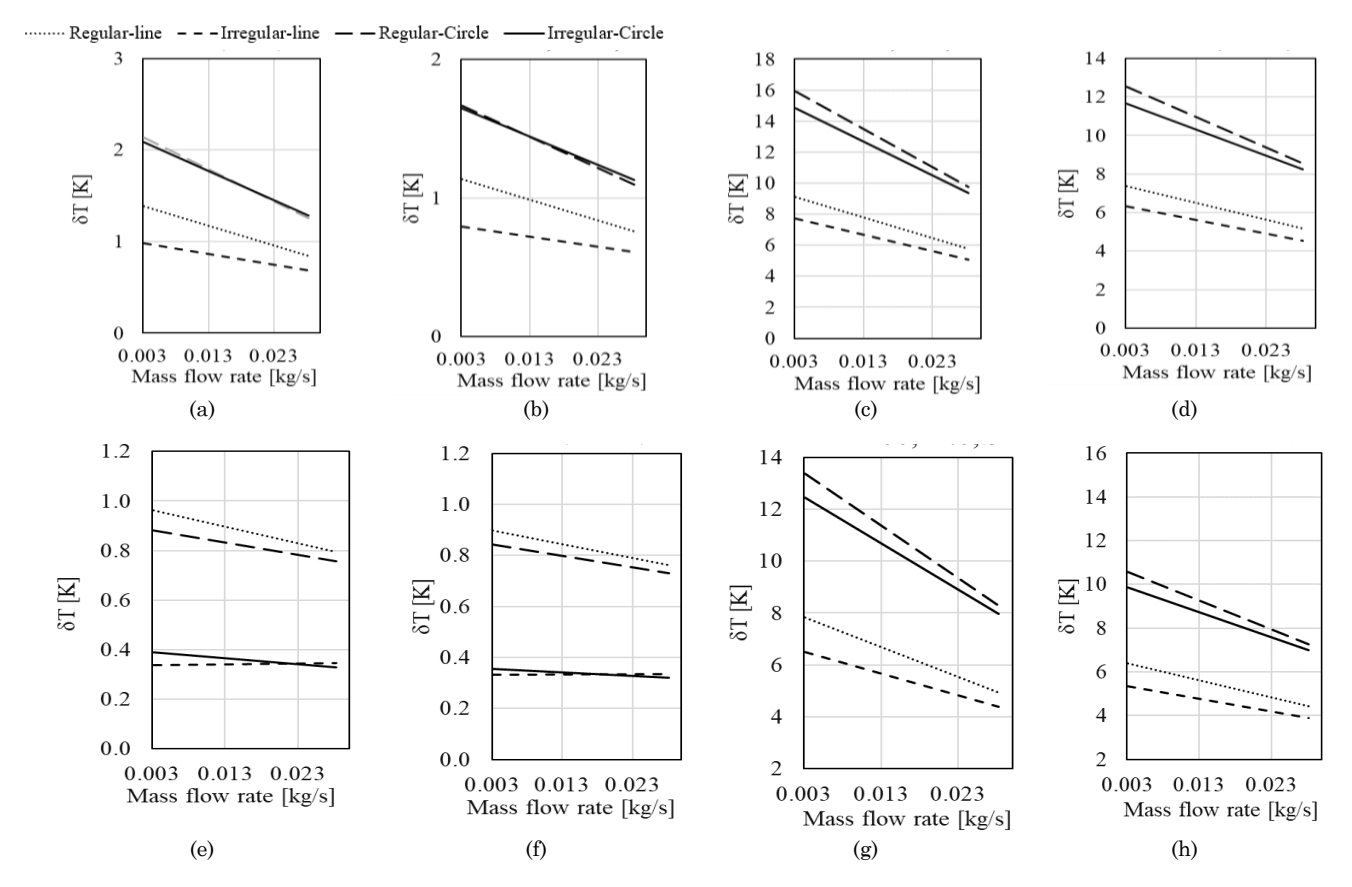


Fig 11. The behaviour of δT of the PV module at Tamb=293K and (a) IS=400 W/m², h_{conv} =2.8 W/m².K, (b) IS=400 W/m², h_{conv} =11.8 W/m².K, (c) IS=1200 W/m², h_{conv} =2.8 W/m².K, and (d) IS=1200 W/m², h_{conv} =11.8 W/m².K, and at H_{amb} =313K under (e) IS=400 W/m², H_{conv} =2.8 W/m².K, (f) IS=400 W/m², H_{conv} =11.8 W/m².K, (g) IS=1200 W/m², H_{conv} =2.8 W/m².K, and (h) IS=1200 W/m², H_{conv} =11.8 W/m².K.

to (a) and (c), respectively. The subfigures (e), (f), (g) and (h) depicts the variation of T_{av} at ambient temperature of 313K. It can be observed that T_{av} rises as T_{amb} increases for all the cases compared to lower T_{amb} . In general, it can be deduced that the four configurations achieve similar average temperatures when subjected to high flow rates. However, at low flow rates, the difference between the four configurations is around 1.5K in the most variant case. Table 2. Indicates the variation of T_{av} for the un-cooled case and the minimum cooled cases among the different configurations considering the highest cooling flow rate.

For the most severe case of the maximum irradiance, maximum ambient temperature, and minimum convection coefficient, the system achieved a reduction of $T_{\rm av}$ by up to

Table 2The variation of T_{av} for the cooled and uncooled cases

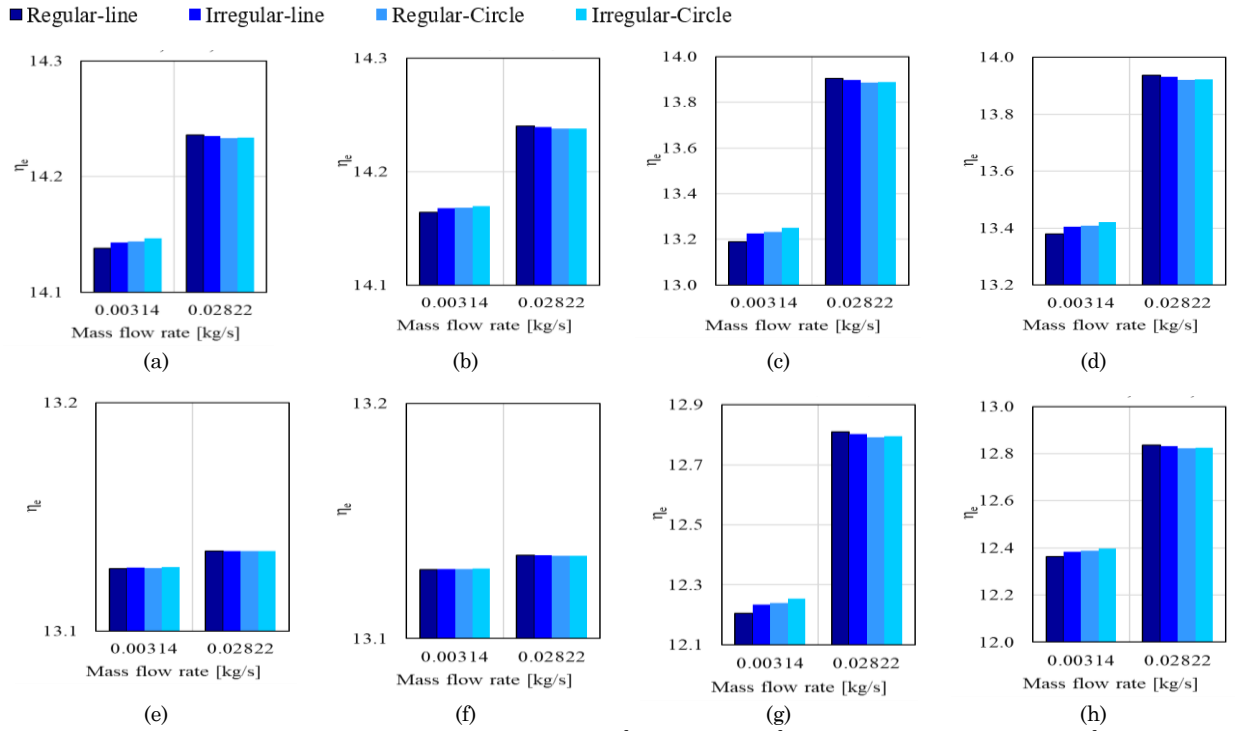
T _{min}	IS [w/m²]	T _{amb} [K]	h _{conv} [W/m².k]	Tav [K]	dT [K]
299.6	1200	293.00	2.80	360.3	60.62
299.1	1200	293.00	11.80	323.1	24.06
318.8	1200	313.00	2.80	367.8	49.06
318.3	1200	313.00	11.80	338.4	20.13
293.9	400	293.00	2.80	303.6	9.70
293.8	400	293.00	11.80	297.2	3.35
313.1	400	313.00	2.80	313.8	0.71
313.1	400	313.00	11.80	313.3	0.27

49.06K, compared to the uncooled system. This reduction reached 60.62K in some cases, as shown in Table 2. The value of the temperature reduction is minimal in the case of the low radiation intensity, which reaches 0.27K.

3.1.3 Temperature un-uniformity distribution.

The study of this parameter is important for preventing the thermal stresses caused by the temperature differences, which can result in different expansion of the PV material and lead to cracks. So, the distribution of the jets is important to keep this parameter as low as possible. Figure 11 shows the temperature un-uniformity factor (δT) variation through the different test cases at an ambient temperature of 293K and 313K. It is observed from Figure 11 that at low ambient temperature, the irregular line distribution achieves the lowest un-uniformity factor of less than 1K at low irradiance of 400 W/m2 (subfigures (a) and (b)), and less than 6K at high radiation power of 1200 W/m² (subfigures (c) and (d)). This behaviour is found to be very near to the regular line configuration in all the tested cases. The circle distribution of the jets shows the highest δT among these configurations. The lowest value of δT reach greater than 1K (subfigures (a) and (b)) and 8K (subfigures (c) and (d) at 400 W/m² and 1200 W/m², respectively. With the increase of the cooling flow rate and the external convection coefficient, this factor decreases due to enhancing the PV cooling.

At high ambient temperatures the values of δT even decrease down to 0.4K and 5K in cases of radiation powers of 400 (subfigures (e) and (f)) and 1200W/m² (subfigures (g) and (h)), respectively, for the irregular distributions. This decrease is



 $\begin{aligned} \textbf{Fig 12}. & \text{The response of } \eta_e \text{ of the PV module at (a) } IS=400 \text{ W/m}^2, h_{conv}=2.8 \text{ W/m}^2.K, Tamb=293K (b) } IS=400 \text{ W/m}^2, h_{conv}=11.8 \\ \text{W/m}^2.K, T_{amb}=293K (c) IS=1200 \text{ W/m}^2, h_{conv}=2.8 \text{ W/m}^2.K, T_{amb}=293K, (d) } IS=1200 \text{ W/m}^2, h_{conv}=11.8 \text{ W/m}^2.K, T_{amb}=293K, (e) } IS=400 \\ \text{W/m}^2, h_{conv}=2.8 \text{ W/m}^2.K, T_{amb}=313K (f) IS=400 \text{ W/m}^2, h_{conv}=11.8 \text{ W/m}^2.K, T_{amb}=313K (g) } IS=1200 \text{ W/m}^2, h_{conv}=2.8 \text{ W/m}^2.K, \\ T_{amb}=313K, (h) IS=1200 \text{ W/m}^2, h_{conv}=11.8 \text{ W/m}^2.K, T_{amb}=313K. \end{aligned}$

caused by the increase of the lower temperature of the PV panel, causing the difference between the higher and lower temperatures to decrease. The irregular-line distribution achieved the best performance for high irradiance powers followed by the regular-line configuration. However, at low radiation power, the irregular line configuration achieves lower δT values at low flow rates, while at high flow rates, the irregular circle configuration achieves lower δT by 0.02K.

As a general comment on the temperature performance of the four tested configurations within the tested parameter ranges, it can be deduced that the irregular-line case is the best case regarding δT , and it is similar to the other configurations in an acceptable range regarding T_{av} .

3.1.4 Energy Efficiencies.

The overall, thermal, and electrical efficiencies of the four tested configurations are explored in the present section, The PV panel's electrical efficiency is inversely proportional to its temperature according to the equation (11). So, it is normal to find that the maximum efficiency of the test cases is achieved at the lowest average temperature configuration. Figure 12 shows the electrical efficiency of the different tested configurations under various test conditions. It is observed that the highest efficiency of 14.2% is achieved at the low ambient temperatures depicted in the subfigures (a), (b), (c), and (d) by the regular line configuration at the highest cooling flow rate. However, at high ambient temperatures, the electrical efficiency decreases to a maximum of 13.13% at the highest cooling flow rate, as shown in subfigures (e), (f), (g), and (h). At low cooling flow rates, the irregular-circular configuration achieves the highest electrical efficiency reaching 13.13%, while the regular-line configuration achieves the highest electrical efficiency of 13.14% under high flow rates.

The value of η_t depends on the quantity of heat collected by the CF with respect to the entering solar radiation energy as expressed by equation (13). Figure 13 shows the variation in η_t of the different test cases under various test parameters. It can be observed that η_t increases with the radiation intensity increase, at low ambient temperature in the subfigures (a), (b), (c) and (d), the thermal efficiency reaches up to 19.7% and 49%, at 400 W/m² (subfigures (a) and (b)) and 1200 W/m² (subfigures (c) and (d)), respectively, for the irregular-line configuration. For higher ambient temperature of 313K, the thermal efficiency reaches up to 45.8% and 42.6% at 400 W/m² (subfigures (e) and (f)) and 1200 W/m² (subfigures (g) and (h)), respectively.

The η_o variation for the PVT system understudy is indicated in figure 14. The value of η_o in this study considers the summation of η_e and η_t and the pumping losses exerted for the CF flow as expressed in equation (14). It is noticed that the increase of the external convection coefficient causes a decrease in η_o . This is caused by the decrease in η_t principally. It is noticed that η_o is affected by η_t more than η_e , due to its higher value in most cases. the overall efficiency reaches up to 33.9% and 49%, at 400 W/m² (subfigures (a) and (b)) and 1200 W/m² (subfigures (c) and (d)), respectively, for the irregular-line configuration.

For higher ambient temperature of 313K, the thermal efficiency reaches up to 14.7% and 55.4% at 400 W/m² (subfigures (e) and (f)) and 1200 W/m² (subfigures (g) and (h)), respectively. In general, the factors affecting η_t have the same effect trend on η_o . This is clear from the inverse proportionality of η_o with T_{amb} and h_{conv} , and its positive proportionality with the radiation intensity and m. The configuration that achieved the

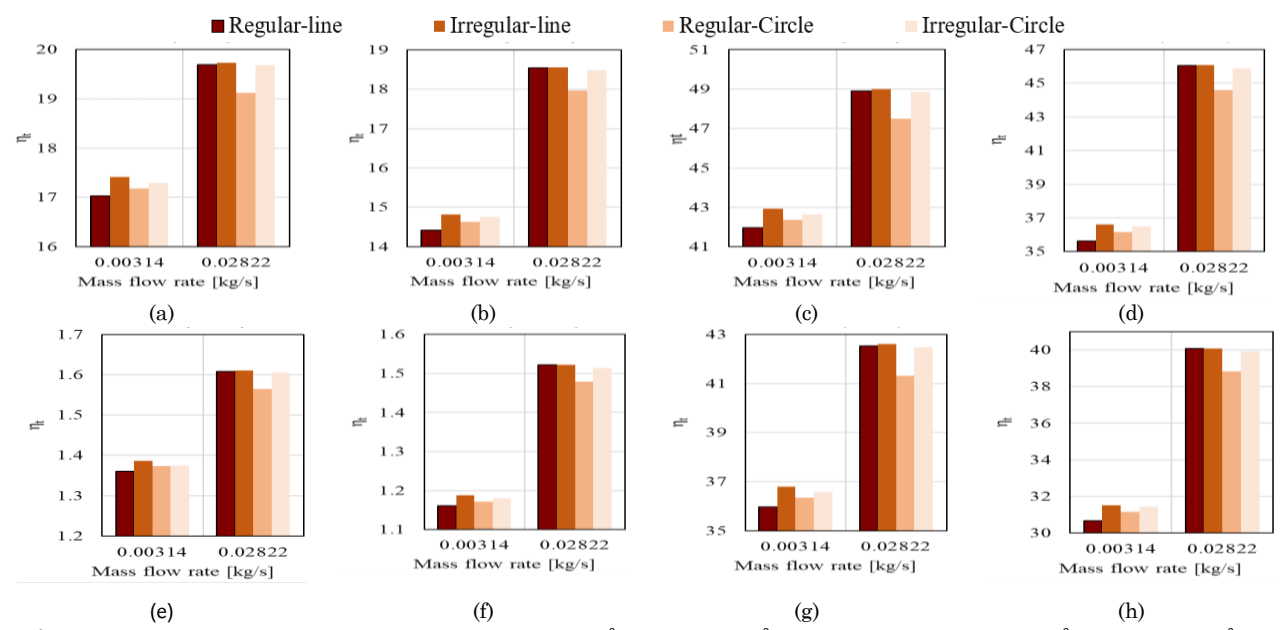


Fig 13. The response of η_t of the PV module at (a) IS=400 W/m², h_{conv} =2.8 W/m².K, T_{amb} =293K (b) IS=400 W/m², h_{conv} =11.8 W/m².K, T_{amb} =293K (c) IS=1200 W/m², h_{conv} =2.8 W/m².K, T_{amb} =293K, (d) IS=1200 W/m², h_{conv} =11.8 W/m².K, T_{amb} =293K, (e) IS=400 W/m², h_{conv} =11.8 W/m².K, h_{conv} =11.8 W/m².K, h_{conv} =11.8 W/m².K, h_{conv} =313K (f) IS=400 W/m², h_{conv} =11.8 W/m².K, h_{conv} =313K. (g) IS=1200 W/m², h_{conv} =2.8 W/m².K, h_{conv} =313K. (h) IS=1200 W/m², h_{conv} =11.8 W/m².K, h_{conv} =11.8 W/

higher overall efficiency is the irregular-line configuration for most of the cases, as observed from Figure 14.

3.2 Optimization Results

In this subsection, the results of the optimum configuration case found in the comparison among the four tested configurations are discussed. The criteria of the comparison are

the lowest δT and the highest η_o . These conditions are met in the irregular-line inlets configuration as indicated in the results discussed in section 3.1. In the present test, some ranges of the boundary parameters are extended to make a solution database that is used for the training of the proposed MFFNN-RSA hybrid model in this research. The solar irradiance power values used are 400, 800, and 1200 W/m². The ambient temperature values are 293, 303, and 313K. The convection coefficient values are

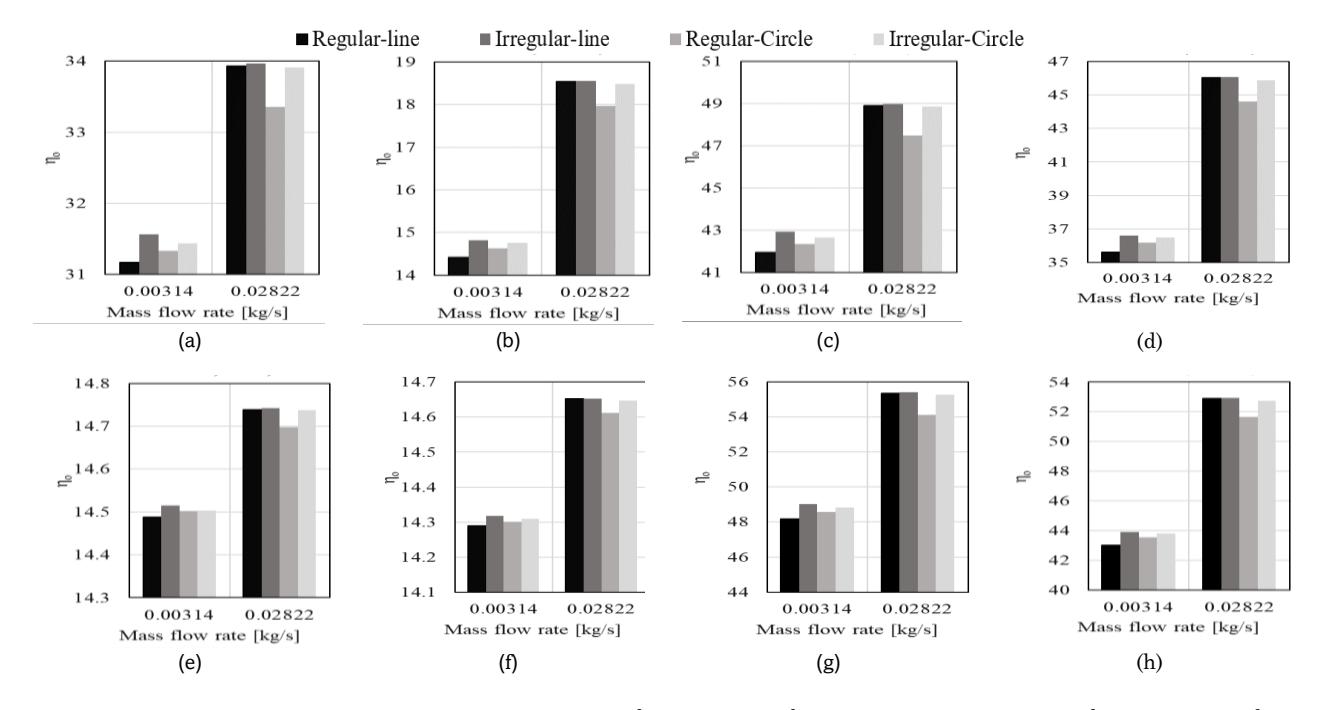


Fig 14. The response of $η_o$ of the PV module at (a) IS=400 W/m², h_{conv} =2.8 W/m².K, T_{amb} =293K (b) IS=400 W/m², h_{conv} =11.8 W/m².K, T_{amb} =293K (c) IS=1200 W/m², h_{conv} =2.8 W/m².K, T_{amb} =293K, (d) IS=1200 W/m², h_{conv} =11.8 W/m².K, h_{conv} =11.8 W/m².K, h_{conv} =11.8 W/m².K, h_{conv} =313K (f) IS=400 W/m², h_{conv} =11.8 W/m².K, h_{conv} =313K (g) IS=1200 W/m², h_{conv} =2.8 W/m².K, h_{conv} =313K, (h) IS=1200 W/m², h_{conv} =11.8 W/m².K, $h_$

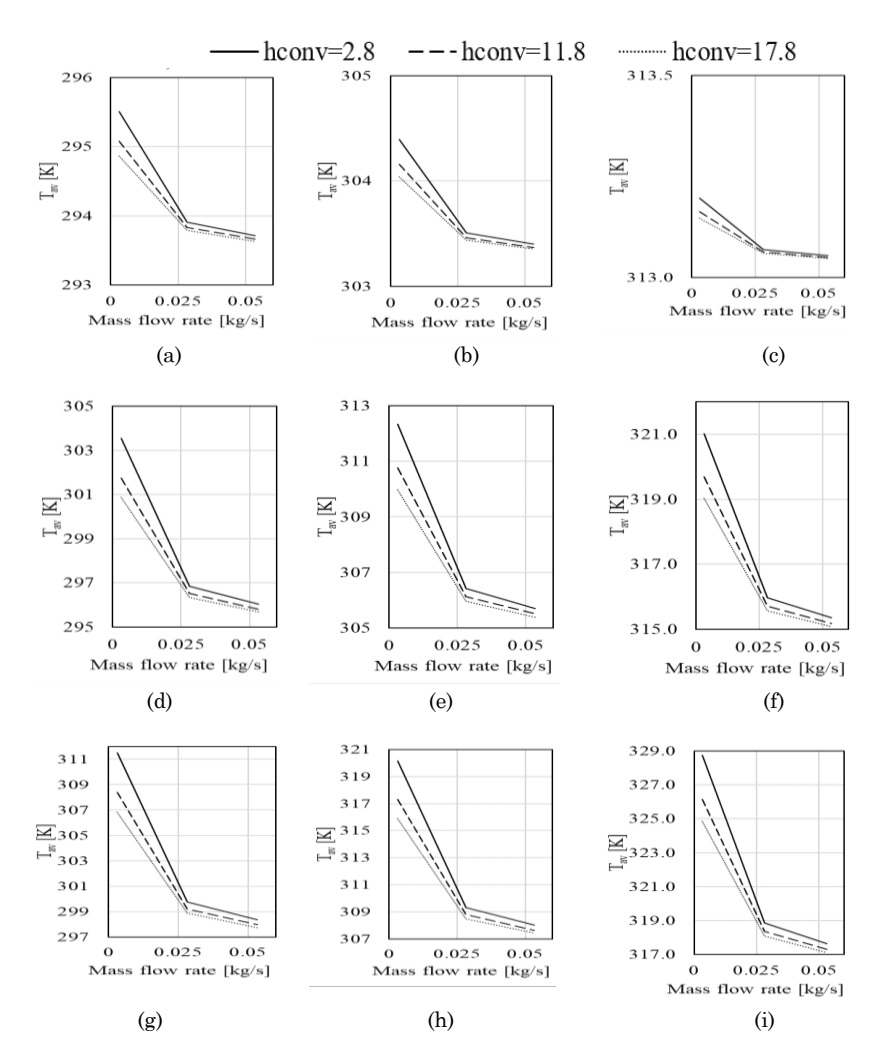


Fig 15. Average temperature variation for cases (a) IS=400 W/m², T_{amb} =293K, (b) IS=400 W/m², T_{amb} =303K, (c) IS=400 W/m², T_{amb} =313K, (d) IS=800 W/m², T_{amb} =293K, (e) IS=800 W/m², T_{amb} =303K, (f) IS=800 W/m², T_{amb} =313K, (g) IS=1200 W/m², T_{amb} =313K, (i) IS=1200 W/m², T_{amb} =313K.

2.8, 11.8, and 17.8 W/ m^2 .K, which are equivalent to wind speeds of 0, 3, and 5 m/s, respectively, according to equation (9). The used \dot{m} are 0.00314, 0.0282, and 0.0533 kg/s.

3.2.1 Average Temperature and Temperature Un-Uniformity.

Figure 15 shows the variation of T_{av} according to different conditions of, convection coefficients, inlet temperatures, solar radiation, and cooling flow rates. The value of T_{av} reaches 293.6K (subfigure a), 303.4K (subfigure b), and 313K (subfigure c), for 400 W/m² and T_{amb} of 293, 303, and 313K, respectively. As the radiation intensity increases to 800 W/m², the value of T_{av} reaches 295.7K (subfigure d), 305.4K (subfigure e), and 315K (subfigure f), for T_{amb} of 293, 303, and 313K, respectively. For the highest radiation intensity of 1200 W/m², the value of T_{av} reaches 297.7K (subfigure g), 307.4K(subfigure h), and 317.1K (subfigure i), for T_{amb} of 293, 303, and 313K, respectively. It is observed that the higher convection coefficient helps in decreasing T_{av} due to the external forced convection effect. Similarly, the higher cooling flow rate helps in decreasing T_{av} . However, the higher radiation intensity and ambient

temperature increase the thermal load on the PV module and as a result increase $T_{\rm av}$.

The variations of δT is shown in Figure 16. It is noticed that the increase of the external convection coefficient enhances the temperature distribution by decreasing δT . This effect is achieved by increasing the cooling flow rate as well. The value of δT reaches 0.51K (subfigure a),0.36K (subfigure b), and 0.33K (subfigure c), for 400 W/m² and T_{amb} of 293, 303, and 313K, respectively. At 800 W/m², the value of δT reaches 2.5K (subfigure d), 1.9K (subfigure e), and 1.7K (subfigure f), for T_{amb} of 293, 303, and 313K, respectively. At 1200 W/m², the value of δT reaches 3.8K (subfigure g), 3.54K (subfigure h), and 3.8K (subfigure i), for T_{amb} of 293, 303, and 313K, respectively.

In general, this behaviour refers to the cooling effect provided by the external wind speed increase and the CF flow rate. The value of δT reaches as maximum as 7.7K at the highest IS of 1200 W/m², and lowest cooling flow rate, ambient temperatures, and lowest convection coefficient. However, as an exceptional case, at radiation of 400 W/m², and T_{amb} of 313K (case c, in figure 16), the increase of the flow rate increases the un-uniformity. This may refer to the heating load caused by the high T_{amb} and h_{conv} with the high cooling provided by the CF. As

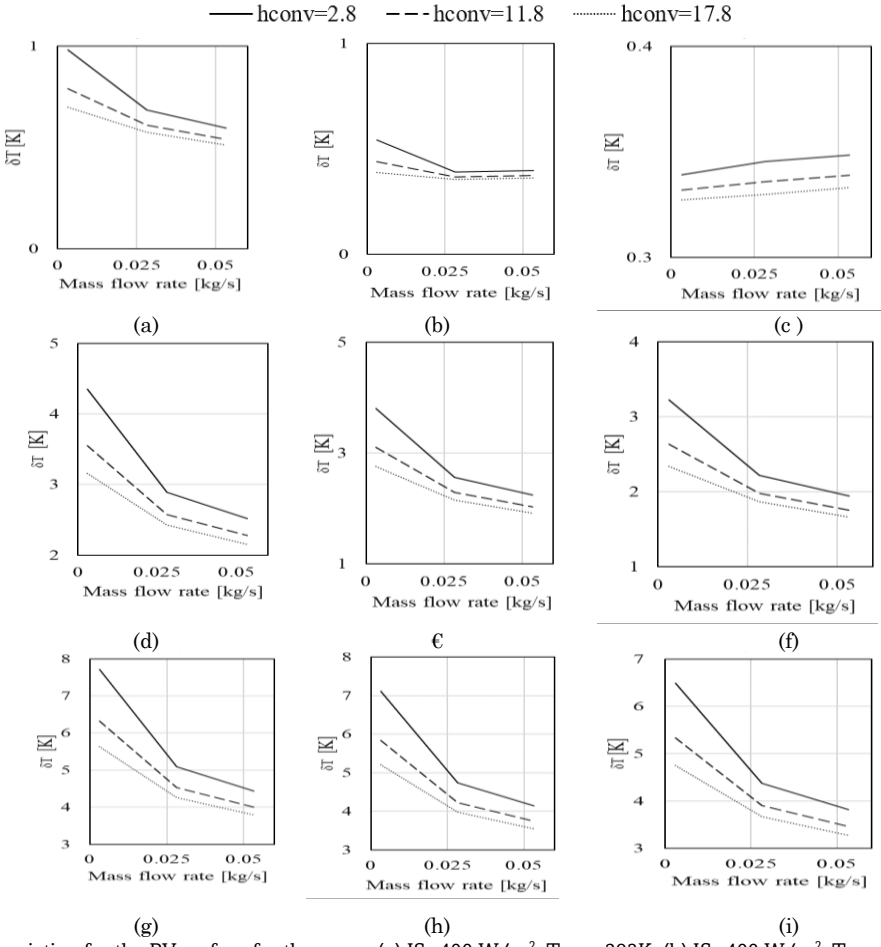


Fig 16. δ T variation for the PV surface for the cases: (a) IS=400 W/m², T_{amb} =293K, (b) IS=400 W/m², T_{amb} =303K, (c) IS=400 W/m², T_{amb} =313K, (d) IS=800 W/m², T_{amb} =293K, € IS=800 W/m², T_{amb} =303K, (f) IS=800 W/m², T_{amb} =313K, (g) IS=1200 W/m², T_{amb} =313K, (h) IS=1200 W/m², T_{amb} =303K, (i) IS=1200 W/m², T_{amb} =313K.

the difference between the external temperature and the CF temperature increases, the un-uniformity increases. As the difference in this case is around 0.5K, as indicated in Figure 16 (c), the difference in the uniformity reached as low as 0.02K according to the flow rate increase. So, this behaviour in that specific case can be neglected as the variation is very low.

3.2.2 Energy Efficiency Variations

In this section, the variations of η_e , η_t , and η_o are discussed. Figure 17. indicates the response of η_e for the different test parameters. It is found that η_e is inversely proportional to $T_{\rm av}$, according to equation (11). The value of η_e reaches 14.25% (subfigure a), 13.7% (subfigure b), and 13.14% (subfigure c), for 400 W/m² and $T_{\rm amb}$ of 293, 303, and 313K, respectively. As the radiation intensity increases to 800 W/m², the value of η_e reaches 14.13% (subfigure d), 13.6% (subfigure e), and 13.23% (subfigure f), for $T_{\rm amb}$ of 293, 303, and 313K, respectively. For the highest radiation intensity of 1200 W/m², the value of η_e reaches 14% (subfigure g), 13.5% (subfigure h), and 12.9% (subfigure i), for $T_{\rm amb}$ of 293, 303, and 313K, respectively.

It is observed that the external convection coefficient and the cooling flow rate have a positive effect in enhancing η_e . However, both of IS and T_{amb} negatively affect η_e . The maximum value of η_e reached 14.25% in the case of the lowest

IS and T_{amb} , with the highest convection coefficient and fluid cooling rate.

The variation in η_t for the test cases is shown in Figure A.1. The value of η_t is observed to be affected positively by IS, and \dot{m} , while affected negatively by h_{conv} and T_{amb}. The value of η_t reaches 20% (subfigure a), 11.2% (subfigure b), and 1.2% (subfigure c), for 400 W/m² and T_{amb} of 293, 303, and 313K, respectively. As the radiation intensity increases to 800 W/m², the value of η_t reaches 42.2% (subfigure d), 37.7% (subfigure e), and 32.8% (subfigure f), for T_{amb} of 293, 303, and 313K, respectively. For the highest radiation intensity of 1200 W/m², the value of η_t reaches 49.6% (subfigure g), 46.5% (subfigure h), and 43.2% (subfigure i), for T_{amb} of 293, 303, and 313K, respectively.

It is clear that the increase in IS increases the energy content incident on the PV module. Additionally, increasing the \dot{m} enhances the convection coefficient, thereby improving the harvesting of this incident energy as thermal energy. The increase of the h_{conv} increases the loss of the thermal energy to the ambient. So, it negatively affects η_t . The ambient temperature increase negatively affects η_t because the inlet CF temperature equals to T_{amb} in the test cases. As the entering temperature of the CF increases, its ability for heat collection decreases. This decreases the collected thermal energy in case of high T_{amb} , and hence decreases η_t . The best η_t in this

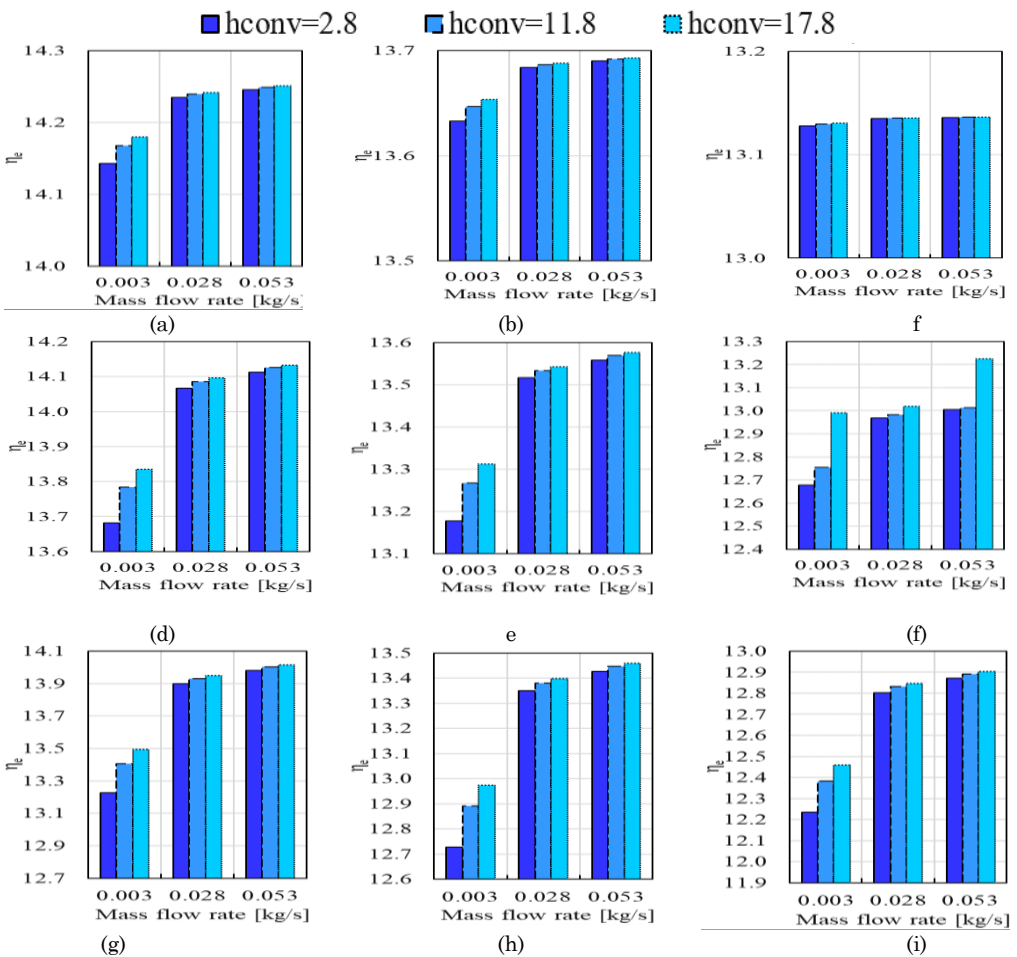


Fig 17. $η_e$ variation for the cases: (a) IS=400 W/m², T_{amb} =293K, (b) IS=400 W/m², T_{amb} =303K, (c) IS=400 W/m², T_{amb} =313K, (d) IS=800 W/m², T_{amb} =293K, ∈ IS=800 W/m², T_{amb} =303K, (f) IS=800 W/m², T_{amb} =313K, (g) IS=1200 W/m², T_{amb} =293K, (h) IS=1200 W/m², T_{amb} =313K.

configuration is 49.5% at the highest \in S and \dot{m} with the lowest T_{amb} and h_{conv} .

The value of η_o is shown in Figure A.2. It is noticed that the cases with lower h_{conv} and lower T_{amb} achieve higher η_o . However, the higher \dot{m} and I, the higher is η_o . This effect is encountered with η_t . The value of η_o reaches 34.2% (subfigure a), 24.9% (subfigure b), and 14.8% (subfigure c), for 400 W/m² and T_{amb} of 293, 303, and 313K, respectively. As the radiation intensity increases to 800 W/m², the value of η_o reaches 56.3% (subfigure d), 51.3% (subfigure e), and 45.8% (subfigure f), for T_{amb} of 293, 303, and 313K, respectively. For the highest radiation intensity of 1200 W/m², the value of η_o reaches 63.5% (subfigure g), 60% (subfigure h), and 56% (subfigure i), for T_{amb} of 293, 303, and 313K, respectively. It is noticed that the system achieved the highest η_o of 63.5% at the case of the highest m and I, and lowest h_{conv} and T_{amb} .

3.3 MFFNN-RSA hybrid model

Several MFFNN architectures are employed, all featuring four inputs (T_{amb} , I, \dot{m} , and h_{conv}) and six outputs (T_{av} , T_{ut} , δT , η_e , η_t , and η_o). However, the number of hidden neurons varies across the models. The fitness function used to assess the optimal neurons' number in the hidden layers relies on the MSE, obtained during the testing and training processes. The most successful network configuration is achieved with 12 and

15 neurons in the first two hidden layers, respectively with six output neurons, resulting in a (4-12-15-6) architecture. A sigmoid transfer function is selected for the two hidden layers.

The output layer of the proposed MFFNN-RSA can minimize the MSE to a final value of 0.4857E-3 within 106 iterations. Figure 18 illustrates the MSE training error convergence diagrams for the MFFNN-RSA. After selecting the appropriate processing steps for the input and target data patterns, the suitable hidden layers' number is selected, and the MFFNN-RSA has been trained.

Figure A.3 depicts the testing, validating, and training regression factor, R, for the proposed MFFNN-RSA hybrid model. The regression factor values for the training, validation, and training are equal to one. This indicates that the proposed MFFNN-RSA hybrid model effectively predicts the true values of PVT performance (T_{av} , T_{ot} , δT , η_e , η_t , and η_o). Furthermore, the RSA attains the optimum architecture of the MFFNN model. Figure A.4 illustrates a comparison between the predicted PVT parameters obtained from the MFFNN-RSA hybrid model and the actual training dataset patterns, which consist of 81 patterns. The figures clearly demonstrate that the predicted parameters derived from the MFFNN-RSA model are closely aligned with the measured parameters.

Once the optimal parameters and structure of the MFFNN-RSA hybrid model are obtained, its performance is evaluated using different datasets that were not utilized during

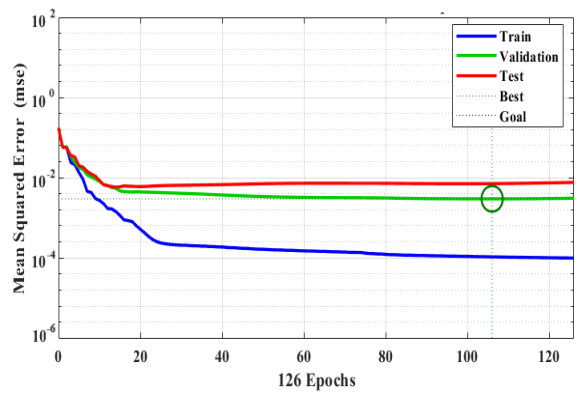


Fig 18. The most convergent training performance of the MFFNN after using the RSA.

the training process. The purpose of this evaluation is to evaluate the capability of the MFFNN-RSA hybrid model to generalize and extrapolate. The proposed MFFNN-RSA hybrid model undergoes testing with various scenarios comprising 19 patterns. In Figure A.5, a visual comparison is presented between the predicted values of T_{av} , T_{ot} , δT , η_e , η_t , and η_o generated by the MFFNN-RSA hybrid model, and the corresponding actual output values. This comparison showcases the MFFNN-RSA hybrid model's capability to predict the desired values accurately.

As shown from Figure A.5, the predicted values closely match the actual values. It indicates that the MFFNN-RSA hybrid model has successfully learned the underlying patterns and relations in the data and can accurately predict the desired values. By combining the power of the MFFNN architecture, the optimization capabilities of the RSA, and rigorous testing

procedures, the MFFNN-RSA hybrid model is able to achieve accurate predictions of the desired values.

4. Economic and Environmental Analysis

As the proposed PVT system is suggested as a cogeneration system for smart buildings, it was beneficial to analyze its economic viability. An economic analysis has been performed for the PVT system understudy, compared to the PV system using the method provided by (Yanhua et al., 2019). The full analysis is shown in Table 3. It can be noticed that the cost of electric energy production is decreased by 11.6%. Moreover, the production of hot water costs 0.02 \$/kW.hr, even if the temperature is not very high, it can be used for preheating applications. The total energy production cost reached 0.0474 \$/kW.hr in the proposed PVT system, compared to 0.1189 \$/kW.hr for the PV system only. The overall yearly energy production reached 582.0 kW.hr/m² which reduces CO₂ emissions by 215.3 kg/m².year according to the CO₂ production rates mentioned in (Hamieh et al., 2022).

5. Conclusions

This work presented novel configurations of jet cooling in a proposed PVT system as a compact solution for smart buildings. The configurations included varying the jets distribution on the cooling plate in a regular or irregular distribution. Moreover, in each distribution, the jets considered as flow inlets were linearly or circularly distributed, while the other jets were considered as outlets. The study compared the four configurations considering the PV average temperature, temperature un-uniformity of the PV, electrical, thermal, and overall efficiency of the system. After the first test, an optimum configuration was identified to be used in the second test set.

Table 3From mic analysis comparison for the PV and PVT system under study

Item	PV system	PVT system 70.00	
Initial cost (P) [\$]	50.00		
Salvage value (S) [\$]	5.00	7.00	
Lifetime (n) [year]	20.0	20.0	
Rate of interest (i)	12.0%	12.0%	
Factor of recovery (RF)	0.134	0.134	
Sink fund factor (SFF)	0.014	0.014	
First Year cost (FYC=RF \times P) [\$]	6.694	9.372	
Yearly salvage value (YSC=SFF \times S) [\$]	0.069	0.097 0.469	
Yearly maintenance cost (YMC=0.05 × FYC) [\$]	0.335		
Totla yearly cost (YC=FYC+YMC-YSV) [\$]	6.959	9.743	
η_e	12.600	14.250	
η_t	0.00	30.03	
Average daily electricity production [kW.hr/m ²]	0.454	0.513 1.081 66.210	
Average daily thermal production [kW.hr/m²]	0.000		
Electricity energy productivity per year[kW.hr/m²]	58.543		
Thermal energy productivity per year [kW.hr/m²]	0.000	139.529	
Electric KW.hr cost [\$/kW.hr]	0.1189	0.1051	
Thermal KW.hr cost [\$/kW.hr]	-	0.0200	
Total kW.hr cost [\$/kW.hr]	0.1189	0.0474	

Then, an MFFNN-RSA hybrid was created for the prediction of the optimum configuration with input parameter ranges of 293 to 313K for ambient temperature, 400, 800, and 1200 $\mbox{W/m}^2$ for irradiance intensity, 0.00314, 0.028, and 0.0533 kg/s for cooling flow rate, and 2.8,11.8, and 17.8 W/m²K for external convection coefficients. The maximum temperature decrease achieved by the presented configuration reached 60.62K compared to the uncooled case while the minimum temperature un-uniformity reached 1K and 6K for 400 and 1000 W/m², respectively. The increase of the ambient temperature found to minimize the temperature un-uniformity in all the cases. The irregular-line configuration achieved the best overall efficiency of 62.9% at a radiation power of 1200 W/m², and cooling flowrate of 0.028 kg/s. The ambient temperature and the radiation intensity were found to increase the average temperature of the PV module, and as a result, the electrical efficiency decreased. However, the high cooling flow rate and external convection coefficient were found to increase the electrical efficiency. The radiation intensity and the flow rate had a positive effect on the overall and thermal efficiencies. In contrast, the ambient temperature and the convection coefficient had a negative effect on the overall and thermal efficiencies. The irregular line configuration achieved an overall efficiency of 63.54% with values of 49.6% and 14.3% of thermal and electrical efficiencies, respectively, considering irradiance intensity of 1200 W/m², cooling flow rate of 0.0533 kg/s, ambient temperature of 293K and external convection coefficient of 2.8 W/m²K. The economic analysis revealed a reduction of the electricity production price by 11.6%. The proposed PVT system's overall energy cost reached 0.0474 \$/kW.hr with a reduction in the yearly Co2 emissions by 215.3 kg/m². The proposed MFFNN-RSA hybrid model minimized the MSE to a final value of 0.4857×10⁻³ within 106 epochs. The regression factor values for the testing, validation, and training of the MFFNN-RSA hybrid model were equal to one. This denotes that it can effectively predict the true values of PVT performance. Combining the MFFNN architecture and the optimization capabilities of the RSA into the MFFNN-RSA hybrid model could achieve accurate predictions of the desired values. The proposed MFFNN-RSA hybrid model had the ability to generalize and extrapolate.

Acknowledgment

The authors extend their appreciation to the deanship of scientific research at Shaqra University for funding this research work through the project number (SU-ANN-2023043).

CrediT authorship contribution statement

Ali Al-Otaibi: Formal analysis, Methodology, Writing – review & editing. Mohamed A. Essa: Methodology, writing – original draft, Software, Validation, Data curation. A. Y. Hatata: Methodology, writing – original draft, ANN model software, Validation, Data curation. Aasem Alabdullatief: Writing – review & editing. Mansoor Alruqi: Formal analysis, Methodology, Writing – review & editing.

Declaration of competing interest

The authors declare that they have no known competing financial interests or personal relationships that could have appeared to influence the work reported in this paper.

References

- Abdel daiem, M. M., Hatata, A., Galal, O. H., Said, N., & Ahmed, D. (2021). Prediction of biogas production from anaerobic codigestion of waste activated sludge and wheat straw using two-dimensional mathematical models and an artificial neural network. *Renewable Energy*, 178, 226–240. https://doi.org/10.1016/J.RENENE.2021.06.050
- Abualigah, L., Elaziz, M. A., Sumari, P., Geem, Z. W., & Gandomi, A. H. (2022). Reptile Search Algorithm (RSA): A nature-inspired meta-heuristic optimizer. *Expert Systems with Applications*, 191, 116158. https://doi.org/10.1016/J.ESWA.2021.116158
- Ahmadi, M. H., Baghban, A., Salwana, E., Sadeghzadeh, M., Zamen, M., Shamshirband, S., & Kumar, R. (2019). Machine Learning Prediction Models of Electrical Efficiency of Photovoltaic-Thermal Collectors. *Preprints*. https://doi.org/10.20944/preprints201905.0033.v1
- Al-Waeli, A. H. A., Kazem, H. A., Yousif, J. H., Chaichan, M. T., & Sopian, K. (2020). Mathematical and neural network modeling for predicting and analyzing of nanofluid-nano PCM photovoltaic thermal systems performance. *Renewable Energy*, 145, 963–980. https://doi.org/10.1016/j.renene.2019.06.099
- Al-Waeli, A. H. A., Sopian, K., Yousif, J. H., Kazem, H. A., Boland, J., & Chaichan, M. T. (2019). Artificial neural network modeling and analysis of photovoltaic/thermal system based on the experimental study. *Energy Conversion and Management*, 186, 368–379. https://doi.org/10.1016/j.enconman.2019.02.066
- Ansys Inc. (2017). Ansys Fluent 17 Theory Guid. Ansys. https://dl.cfdexperts.net/cfd_resources/Ansys_Documentation/Fluent/Ansys_Fluent_Theory_Guide.pdf
- Baloch, A. A. B., Bahaidarah, H. M. S., Gandhidasan, P., & Al-Sulaiman, F. A. (2015). Experimental and numerical performance analysis of a converging channel heat exchanger for PV cooling. *Energy Conversion and Management*, 103, 14–27. https://doi.org/https://doi.org/10.1016/j.enconman.2015.0 6.018
- Bayrak, F., Oztop, H. F., & Selimefendigil, F. (2019). Effects of different fin parameters on temperature and efficiency for cooling of photovoltaic panels under natural convection. *Solar Energy*, 188, 484–494. https://doi.org/https://doi.org/10.1016/j.solener.2019.06.0
- Büyükalaca, O., Kılıç, H. M., Olmuş, U., Güzelel, Y. E., & Çerçi, K. N. (2023). Numerical investigation and ANN modeling of performance for hexagonal boron Nitride-water nanofluid PVT collectors. *Thermal Science and Engineering Progress*, 43, 101997. https://doi.org/10.1016/j.tsep.2023.101997
- Cao, Y., Kamrani, E., Mirzaei, S., Khandakar, A., & Vaferi, B. (2022). Electrical efficiency of the photovoltaic/thermal collectors cooled by nanofluids: Machine learning simulation and optimization by evolutionary algorithm. *Energy Reports*, 8, 24–36. https://doi.org/10.1016/j.egyr.2021.11.252
- Chaibi, Y., Malvoni, M., Rhafiki, T. El, Kousksou, T., & Zeraouli, Y. (2021). Artificial neural-network based model to forecast the electrical and thermal efficiencies of PVT air collector systems.

 Cleaner Engineering and Technology, 4, 100132.
 https://doi.org/10.1016/j.clet.2021.100132
- Delfani, S., Esmaeili, M., & Karami, M. (2019). Application of artificial neural network for performance prediction of a nanofluid-based direct absorption solar collector. *Sustainable Energy Technologies and Assessments*, 36, 100559. https://doi.org/10.1016/j.seta.2019.100559
- Dimri, N., Tiwari, A., & Tiwari, G. N. (2019). Comparative study of photovoltaic thermal (PVT) integrated thermoelectric cooler (TEC) fluid collectors. *Renewable Energy*, 134, 343–356. https://doi.org/10.1016/j.renene.2018.10.105
- Duffie, J. A., & Beckman, W. A. (2013). Solar Engineering of Thermal Processes. Wiley. https://doi.org/10.1002/9781118671603
- Dwivedi, P., Sudhakar, K., Soni, A., Solomin, E., & Kirpichnikova, I. (2020). Advanced cooling techniques of P.V. modules: A state of art. *Case Studies in Thermal Engineering*, 21, 100674. https://doi.org/https://doi.org/10.1016/j.csite.2020.100674

- Elminshawy, N. A. S., Mohamed, A. M. I., Morad, K., Elhenawy, Y., & Alrobaian, A. A. (2019). Performance of PV panel coupled with geothermal air cooling system subjected to hot climatic. *Applied Thermal Engineering*, 148, 1–9. https://doi.org/https://doi.org/10.1016/j.applthermaleng.2 018.11.027
- Essa, M. A., Alshqirate, A. A., & Hatata, A. Y. (2023). Analyzing the effect of normally distributed cooling channels on a photovoltaic thermal solar unit. *Journal of Cleaner Production*, 426, 139015. https://doi.org/10.1016/J.JCLEPRO.2023.139015
- Ewe, W. E., Fudholi, A., Sopian, K., Moshery, R., Asim, N., Nuriana, W., & Ibrahim, A. (2022). Thermo-electro-hydraulic analysis of jet impingement bifacial photovoltaic thermal (JIBPVT) solar air collector. *Energy*, 254, 124366. https://doi.org/10.1016/J.ENERGY.2022.124366
- Gharzi, M., Arabhosseini, A., Gholami, Z., & Rahmati, M. H. (2020).

 Progressive cooling technologies of photovoltaic and concentrated photovoltaic modules: A review of fundamentals, thermal aspects, nanotechnology utilization and enhancing performance.

 Solar Energy, 211, 117–146. https://doi.org/10.1016/J.SOLENER.2020.09.048
- Gunasekar, N., Mohanraj, M., & Velmurugan, V. (2015). Artificial neural network modeling of a photovoltaic-thermal evaporator of solar assisted heat pumps. *Energy*, *93*, 908–922. https://doi.org/10.1016/J.ENERGY.2015.09.078
- Hamieh, A., Rowaihy, F., Al-Juaied, M., Abo-Khatwa, A. N., Afifi, A. M., & Hoteit, H. (2022). Quantification and analysis of CO2 footprint from industrial facilities in Saudi Arabia. *Energy Conversion and Management: X, 16,* 100299. https://doi.org/10.1016/J.ECMX.2022.100299
- Hasan, H. A., Sopian, K., & Fudholi, A. (2018). Photovoltaic thermal solar water collector designed with a jet collision system. *Energy*, 161, 412–424. https://doi.org/10.1016/J.ENERGY.2018.07.141
- Javidan, M., & Moghadam, A. J. (2021). Experimental investigation on thermal management of a photovoltaic module using water-jet impingement cooling. *Energy Conversion and Management*, 228, 113686.
 - https://doi.org/https://doi.org/10.1016/j.enconman.2020.1 13686
- Kalani, H., Sardarabadi, M., & Passandideh-Fard, M. (2017). Using artificial neural network models and particle swarm optimization for manner prediction of a photovoltaic thermal nanofluid based collector. Applied Thermal Engineering, 113, 1170–1177.
 - https://doi.org/10.1016/j.applthermaleng.2016.11.105
- Kalateh, M. R., Kianifar, A., & Sardarabadi, M. (2022). Energy, exergy, and entropy generation analyses of a water-based photovoltaic thermal system, equipped with clockwise counter-clockwise twisted tapes: An indoor experimental study. *Applied Thermal Engineering*, 215, 118906. https://doi.org/https://doi.org/10.1016/j.applthermaleng.2 022.118906
- Kazemian, A., Khatibi, M., Ma, T., Peng, J., & Hongxing, Y. (2023). A thermal performance-enhancing strategy of photovoltaic thermal systems by applying surface area partially covered by solar cells. *Applied Energy*, 329, 120209. https://doi.org/https://doi.org/10.1016/j.apenergy.2022.12 0209
- Khalaf, A. E., Eleiwi, M. A., & Yassen, T. A. (2023). Enhancing the overall performance of the hybrid solar photovoltaic collector by open water cycle jet-cooling. *Renewable Energy*, 208, 492– 503. https://doi.org/10.1016/J.RENENE.2023.02.122
- Khan, M. K., Zafar, M. H., Rashid, S., Mansoor, M., Moosavi, S. K. R., & Sanfilippo, F. (2023). Improved Reptile Search Optimization Algorithm: Application on Regression and Classification Problems. Applied Sciences, 13(2). https://doi.org/10.3390/app13020945
- Koohestani, S. S., Nižetić, S., & Santamouris, M. (2023). Comparative review and evaluation of state-of-the-art photovoltaic cooling technologies. *Journal of Cleaner Production*, 406, 136953. https://doi.org/10.1016/J.JCLEPRO.2023.136953

- Leema, N., Nehemiah, H. K., & Kannan, A. (2016). Neural network classifier optimization using Differential Evolution with Global Information and Back Propagation algorithm for clinical datasets. *Applied Soft Computing*, 49, 834–844. https://doi.org/10.1016/J.ASOC.2016.08.001
- Li, Y., Wang, Z., Yang, J., & Liu, H. (2020). Thermal and hydraulic characteristics of microchannel heat sinks with cavities and fins based on field synergy and thermodynamic analysis. Applied Thermal Engineering, 175, 115348. https://doi.org/10.1016/J.APPLTHERMALENG.2020.11534
- Nahar, A., Hasanuzzaman, M., & Rahim, N. A. (2017). Numerical and experimental investigation on the performance of a photovoltaic thermal collector with parallel plate flow channel under different operating conditions in Malaysia. *Solar Energy*, 144, 517–528. https://doi.org/https://doi.org/10.1016/j.solener.2017.01.0 41
- Özcan, Z., Gülgün, M., Şen, E., Çam, N. Y., & Bilir, L. (2021). Cooling channel effect on photovoltaic panel energy generation. *Solar Energy*, 230, 943–953. https://doi.org/10.1016/J.SOLENER.2021.10.086
- Patil, M., Sidramappa, A., Shetty, S. K., & Hebbale, A. M. (2023). Experimental study of solar PV/T panel to increase the energy conversion efficiency by air cooling. *Materials Today:* Proceedings. https://doi.org/10.1016/J.MATPR.2023.05.007
- Shahsavar, A., & Arici, M. (2023). Energy and exergy analysis and optimization of a novel heating, cooling, and electricity generation system composed of PV/T-heat pipe system and thermal wheel. *Renewable Energy*, 203, 394–406. https://doi.org/10.1016/J.RENENE.2022.12.071
- Shen, C., Zhang, Y., Zhang, C., Pu, J., Wei, S., & Dong, Y. (2021). A numerical investigation on optimization of PV/T systems with the field synergy theory. *Applied Thermal Engineering*, 185, 116381.
 - https://doi.org/https://doi.org/10.1016/j.applthermaleng.2 020.116381
- Song, Z., Xue, Y., Jia, B., & He, Y. (2023). Introduction of the rectangular hole plate in favor the performance of photovoltaic thermal solar air heaters with baffles. *Applied Thermal Engineering*, 220, 119774. https://doi.org/https://doi.org/10.1016/j.applthermaleng.2 022.119774
- Talaat, M., Farahat, M. A., Mansour, N., & Hatata, A. Y. (2020). Load forecasting based on grasshopper optimization and a multilayer feed-forward neural network using regressive approach. *Energy*, 196, 117087. https://doi.org/10.1016/J.ENERGY.2020.117087
- Tiwari, A., Sodha, M. S., Chandra, A., & Joshi, J. C. (2006). Performance evaluation of photovoltaic thermal solar air collector for composite climate of India. *Solar Energy Materials and Solar Cells*, 90(2), 175–189. https://doi.org/https://doi.org/10.1016/j.solmat.2005.03.00
- Wei Wang Ming Li, R. H. E. H. M. en J., & Feng, Z. (2017). Optimization of thermal performance of the parabolic trough solar collector systems based on GA-BP neural network model. *International Journal of Green Energy*, 14(10), 819–830. https://doi.org/10.1080/15435075.2017.1333433
- Yanhua, L., Wengang, H., Hongwen, Y., zheng jian, & Mingxin, L. (2019). Performance and economic evaluation of evacuated tube solar collector with auxiliary electric heater for rural heating. *Energy Procedia*, 158, 186–191. https://doi.org/https://doi.org/10.1016/j.egypro.2019.01.06
- Yildirim, M. A., Cebula, A., & Sułowicz, M. (2022). A cooling design for photovoltaic panels – Water-based PV/T system. *Energy*, 256, 124654. https://doi.org/https://doi.org/10.1016/j.energy.2022.1246
- Yousif, J. H., Kazem, H. A., Alattar, N. N., & Elhassan, I. I. (2019). A comparison study based on artificial neural network for assessing PV/T solar energy production. *Case Studies in*

- *Thermal Engineering*, *13*, 100407. https://doi.org/10.1016/J.CSITE.2019.100407
- Yuan, Q., Zhang, Y., Dai, X., & Zhang, S. (2022). A Modified Reptile Search Algorithm for Numerical Optimization Problems. *Computational Intelligence and Neuroscience, 2022*, 9752003. https://doi.org/10.1155/2022/9752003
- Zhang, Q., He, S., Song, T., Wang, M., Liu, Z., Zhao, J., Gao, Q., Huang, X., Han, K., Qi, J., Gao, M., & Shi, Y. (2023). Modeling of a PV system by a back-mounted spray cooling section for
- performance improvement. *Applied Energy*, *332*, 120532. https://doi.org/https://doi.org/10.1016/j.apenergy.2022.12 0532
- Zhang, Y., Shen, C., Zhang, C., Pu, J., Yang, Q., & Sun, C. (2022). A novel porous channel to optimize the cooling performance of PV modules. *Energy and Built Environment*, 3(2), 210–225. https://doi.org/https://doi.org/10.1016/j.enbenv.2021.01.0



© 2024. The Author(s). This article is an open access article distributed under the terms and conditions of the Creative Commons Attribution-ShareAlike 4.0 (CC BY-SA) International License (http://creativecommons.org/licenses/by-sa/4.0/)

Appendix A

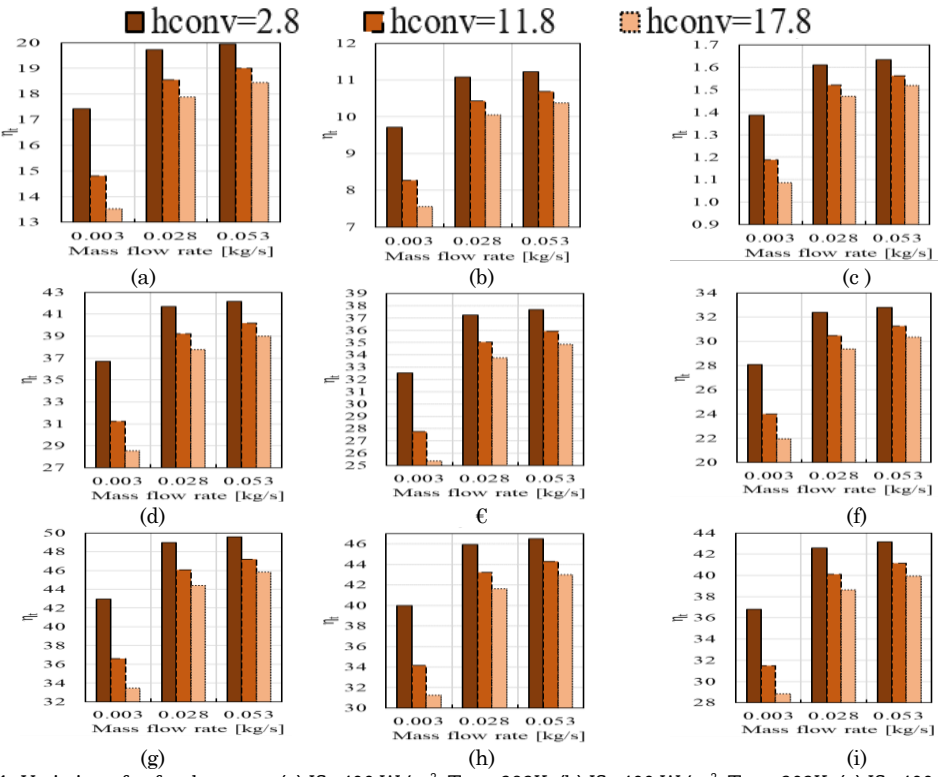


Fig A.1. Variation of η_t for the cases: (a) IS=400 W/m², T_{amb} =293K, (b) IS=400 W/m², T_{amb} =303K, (c) IS=400 W/m², T_{amb} =313K, (d) IS=800 W/m², T_{amb} =293K, ∈ IS=800 W/m², T_{amb} =303K, (f) IS=800 W/m², T_{amb} =313K, (g) IS=1200 W/m², T_{amb} =313K, (i) IS=1200 W/m², T_{amb} =313K.

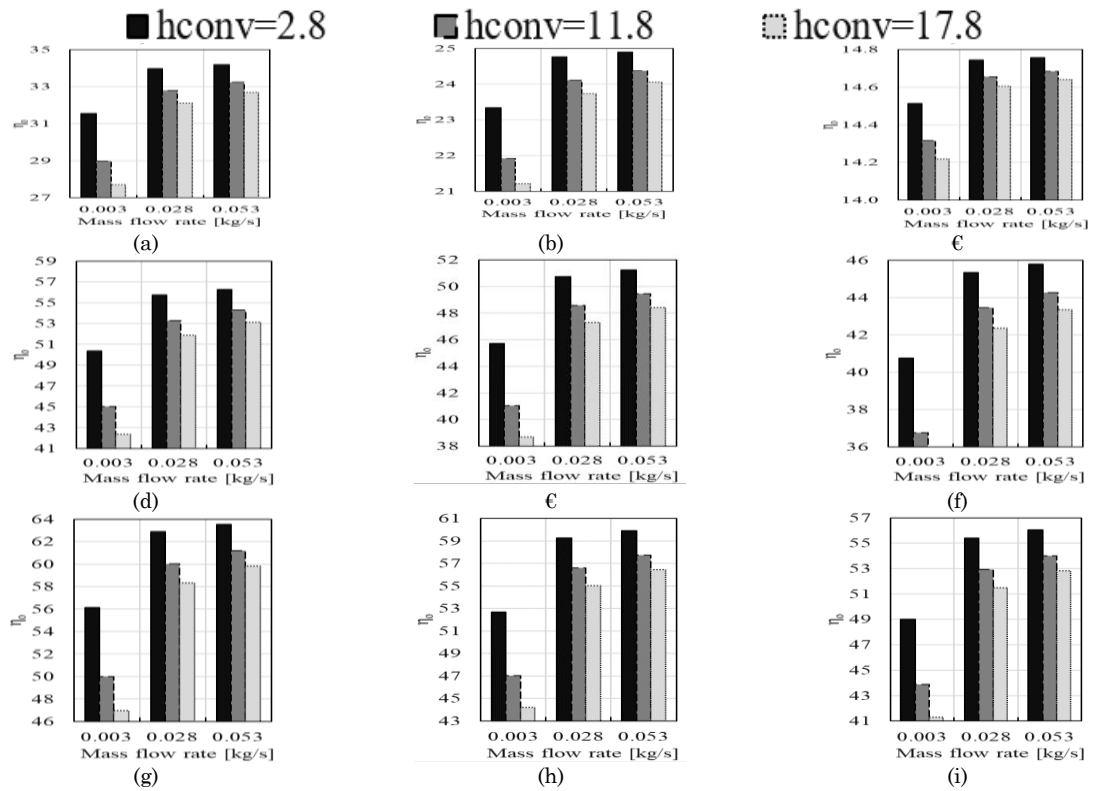


Fig A.2. $η_o$ variation for the cases: (a) IS=400 W/m², T_{amb} =293K, (b) IS=400 W/m², T_{amb} =303K, (c) IS=400 W/m², T_{amb} =313K, (d) IS=800 W/m², T_{amb} =293K, ∈ IS=800 W/m², T_{amb} =303K, (f) IS=800 W/m², T_{amb} =313K, (g) IS=1200 W/m², T_{amb} =293K, (h) IS=1200 W/m², T_{amb} =303K, (i) IS=1200 W/m², T_{amb} =313K.

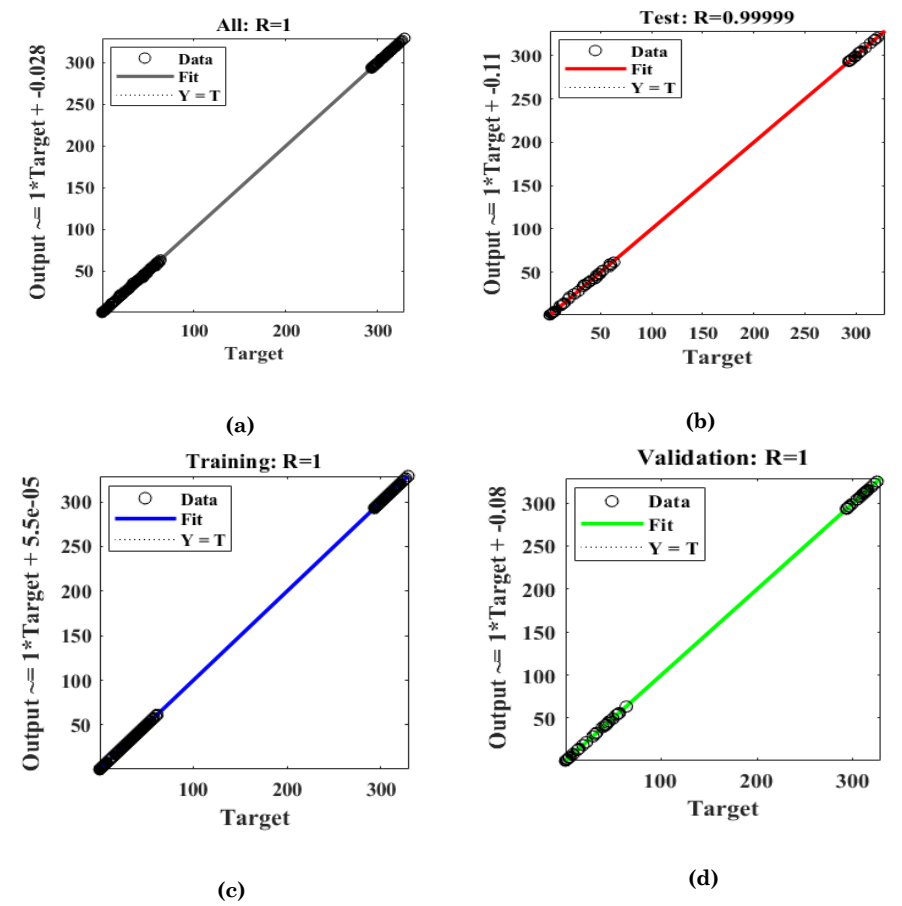


Fig A.3. The regression diagram for the MFFNN-RSA (a) training, (b) validation, (c) testing, and (d) overall stages

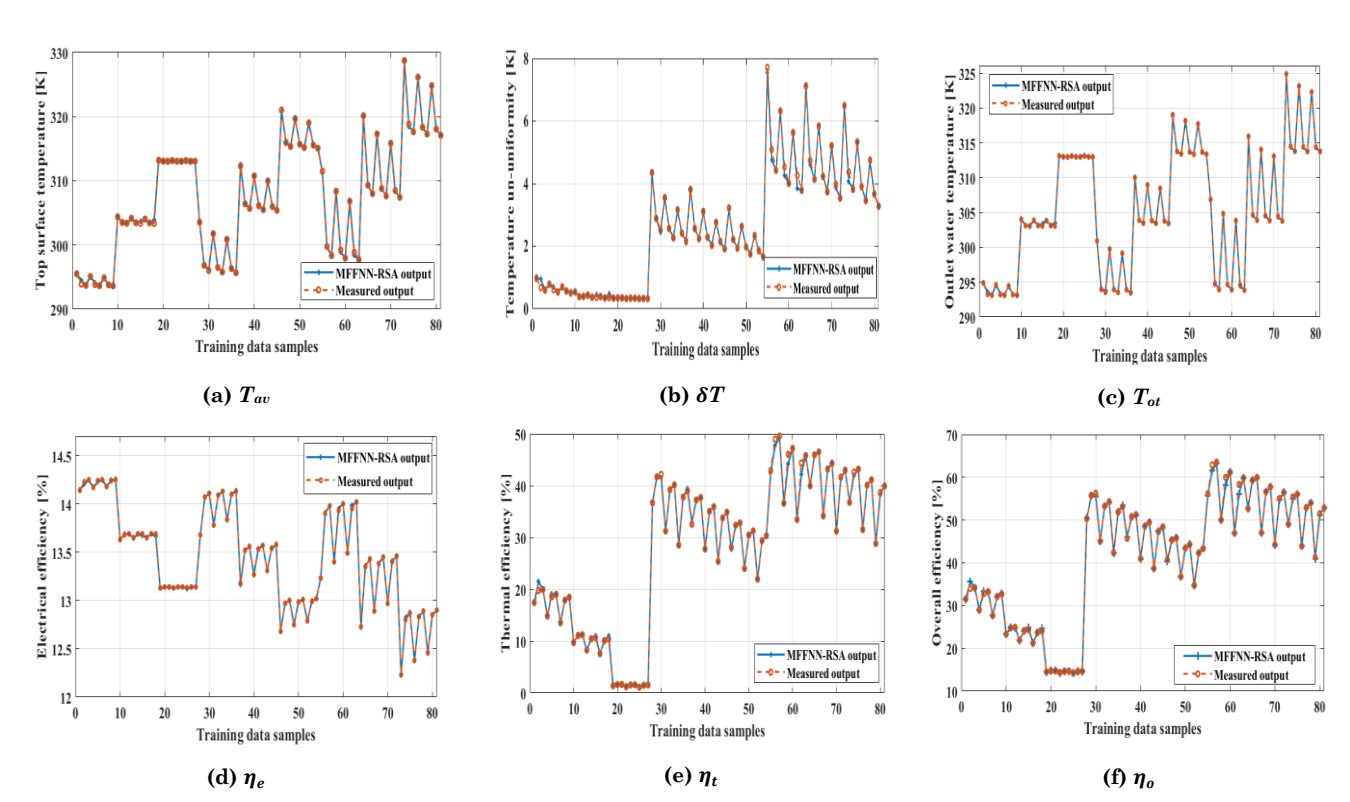


Fig A.4. Comparison between the MFFNN-RSA hybrid model and the training data.

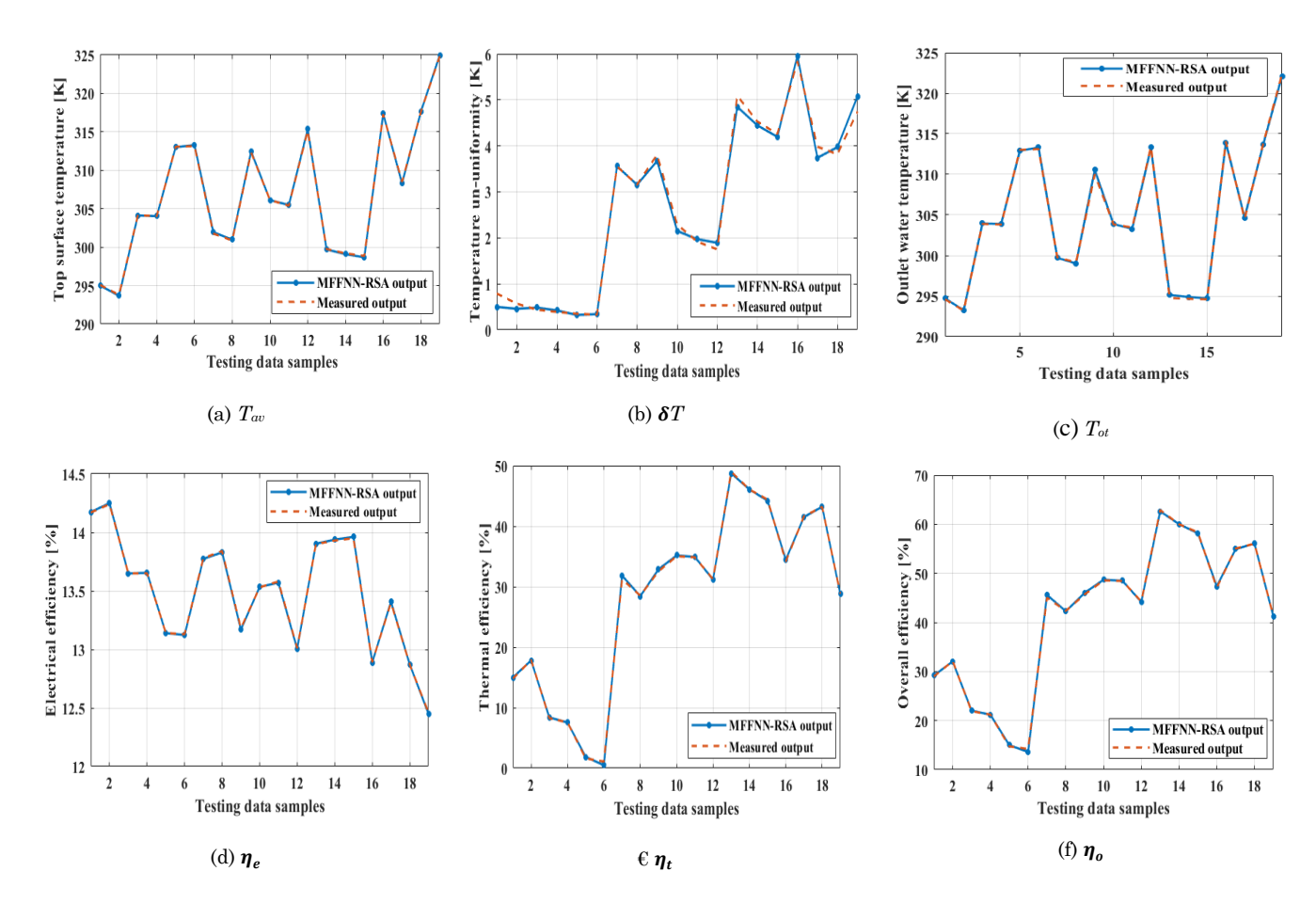


Fig A.5. Comparison between the MFFNN-RSA hybrid model and testing data output.